Engineering Solutions to Scale Up Trapped-Ion System

Le Minh Anh Nguyen

A thesis
submitted in partial fulfillment of the
requirements for the degree of

Masters of Science

University of Washington

2026

Committee:

Sara Mouradian, Chair

Maxwell Parsons

Program Authorized to Offer Degree:
Department of Electrical and Computer Engineering

©Copyright 2026
Le Minh Anh Nguyen

University of Washington

Abstract

Engineering Solutions to Scale Up Trapped-Ion System

Le Minh Anh Nguyen

Chair of the Supervisory Committee:

Sara Mouradian
Department of Electrical and Computer Engineering

Trapped-ion quantum processors offer some of the lowest gate error rates among qubit platforms, encoding quantum information in ionic energy levels and entangling qubits via shared motional modes. Despite this maturity, scaling to large qubit numbers while maintaining high-fidelity control remains a central challenge. This thesis addresses two key bottlenecks in laser-based trapped-ion systems: trap geometry and laser delivery.

The first contribution is a quantitative framework for evaluating trap geometries with respect to scalability, applied to three electrode designs: a conventional surface trap, a "gnd-surface" multi-wafer trap, and a symmetric "cross-rf" multi-wafer trap [1]. Multi-wafer designs, particularly the cross-rf trap, show substantial improvements in harmonicity, trap depth, radial trap frequency, and heating rate. However, the gnd-surface trap is identified as the most promising path to scaling due to its significantly simpler fabrication.

The second contribution is the initial implementation of a photonic integrated circuit (PIC) for scalable laser delivery to $^{40}Ca^{+}$ ions. Operating at 729 nm, the PIC supports slow thermal tuning and fast nanosecond-scale modulation, with a path toward FPGA integration. Coupling of a frequency-stabilized laser into the PIC was demonstrated.

Together, these contributions advance a modular architecture for trapped-ion quantum computation in which trap geometry and optical control are each independently engineered for large-scale operation.

TABLE OF CONTENTS

Page

List of Figures ii

Glossary vi

Chapter 1: Introduction 1

Chapter 2: Theory 4
2.1 Physical Implementation 4
2.2 Single-qubit (1Q) Gate 15
2.3 Two-qubit (2Q) Gate 19

Chapter 3: Trap Geometry 29
3.1 Trap Geometries and Simulation Methods 29
3.2 Figures of merits 34
3.3 Expected Experimental Performance 39
3.4 Practicality 43

Chapter 4: Light Delivery 46
4.1 Photonic Integrated Circuit 47
4.2 Optical Setup and Characterization 49
4.3 Next Steps: FPGA Integration and Experimental Application 51

Chapter 5: Conclusions and Outlook 53

Bibliography 55

Appendix A: Useful mathematical definitions 67
A.1 Pauli Matrices 67

LIST OF FIGURES

Figure Number — Page

2.1 (a) The Bloch sphere provides a geometric representation of all possible pure states of a qubit, parameterized by polar angle θ and azimuthal angle φ. The north and south poles correspond to the computational basis states $|0\rangle$ and $|1\rangle$. (b) Relevant energy levels of the $^{40}Ca^{+}$ ion. The qubit is encoded in the $4s^2S_{1/2}$ ground state $|0\rangle$ and the metastable $3d^2D_{5/2}$ state $|1\rangle$, which are coupled by the 729 nm electric quadrupole "clock" transition used for qubit manipulation. The long natural lifetime of the $D_{5/2}$ state ($\tau = 1.17$ s) suppresses spontaneous emission. State-dependent fluorescence on the 397 nm $S_{1/2} \leftrightarrow P_{1/2}$ transition provides qubit readout: an ion in $|0\rangle$ scatters photons ("bright"), while an ion shelved in $|1\rangle$ remains dark. 5

2.2 (a) The four-rod electrode geometry of a linear Paul trap, where two opposing electrodes are driven by a radio-frequency (rf) source of $V_{\mathrm{rf}} \cos(\Omega_{\mathrm{rf}} t + \phi)$, while the remaining two electrodes are held at ground. The resulting time-dependent quadrupole field creates a net radial confinement when Ω_{rf} is much larger than the ion's motion. In this limit, the micromotion driven at Ω_{rf} averages out and the ion undergoes slow secular harmonic oscillation at frequency ω_r about the RF null at the trap center. (b) Representative radial pseudopotential at the axial midpoint ($z = 0$) of a linear Paul trap similar to (a). The pseudopotential approximation replaces the time-varying field with an effective static potential, valid when $\omega_r \ll \Omega_{\mathrm{rf}}$, and forms a harmonic well for ion confinement. 7

2.3 (a) Energy level diagram of the quantum harmonic oscillator (QHO) with Hamiltonian $\hat{\mathcal{H}}_{\mathrm{QHO}}$ from (2.40), describing the secular motion of a trapped ion at frequency ω_r. The equally spaced levels $\hbar\omega_r(n+1/2)$ define the Fock states $|n\rangle$, with ladder operators $\hat{a}$ and $\hat{a}^\dagger$ stepping between them. The overlaid wavefunctions $\psi_n(r)$ from (2.44) show the growing spatial extent and node count with n, reflecting increasing positional uncertainty and kinetic energy. (b) Phase-space representation of the displacement operator $\hat{D}(\alpha)$ acting on the motional ground state $|0\rangle_n$. The complex displacement α encodes both the magnitude $|\alpha|$ and direction of the shift, producing a coherent state $|\alpha\rangle_n$ at $(\mathrm{Re}(\alpha), \mathrm{Im}(\alpha)) = (0.5, 0.5)$. 12

2.4 (a) Spin-motion energy level diagram of the Mølmer-Sørensen (MS) interaction. Each ion is simultaneously driven by two lasers, one on the blue sideband ($\Omega_{\text{bsb}}^{(1,2)}$) and the other on the red sideband ($\Omega_{\text{rsb}}^{(1,2)}$), each detuned by Δ from the motional sideband frequency. The four resulting coupling paths interfere constructively to entangle the two-qubit spin states while leaving the net motional state unchanged. (b) Phase-space trajectories of the spin-dependent displacement from (2.119). The $|00\rangle$ and $|11\rangle$ spin components trace closed circular orbits of equal radius but opposite orientation, each accumulating a geometric phase proportional to the enclosed area. Loop closure at $\alpha(T) = 0$ guarantees the motional mode disentangles from the qubit register at the gate time. (c) Population dynamics under the MS interaction, initialized in $|00\rangle$. The populations P_{00} and P_{11} undergo coherent oscillation and at t_{gate} (2.121), $P_{00} = P_{11} = 0.5$ and $P_{\text{mixed}} = 0$, indicating the target maximally entangled Bell state has been prepared. 22

3.1 (a-c) Electrode geometries for the surface trap, "gnd-surface" trap, and "cross-rf" trap, respectively. rf electrodes are shown in red, dc electrodes in blue, and grounded electrodes in black. The parameter h denotes the wafer separation in the two multi-wafer designs and is varied. (d-f) Two-dimensional pseudopotential maps of the x-y radial cross-section at $z = 0$ for the geometries in (a-c), respectively. The rf-null point marks the ion equilibrium position above the electrode plane define as $y = d$. The distance from the ion to the nearest electrode-surface is r_0 and x_0 is the distance from nearest rf rail to the origin. (g-i) One-dimensional pseudopotential slices at $z = 0$, $x = 0$ for (a-b), and along $r = \sqrt{x^2 + y^2}$ for (c), used to extract the trap depth. The red dashed line marks the saddle point of the pseudopotential, whose value relative to the rf-null minimum defines the trap depth and sets the maximum ion kinetic energy before escape. 31

3.2 (a) Mean phonon number $\langle n \rangle$ as a function of time during the MS gate, tracing the phase-space loop of Fig. 2.4(b). The motional excitation increases and returns to zero at t_{gate}, with a maximum occupation of $\langle n \rangle = 0.5$. (b) Radial trap frequency ω_{rad} as a function of mean phonon number $\langle n \rangle$, fitted with quadratic ($ax^2 + bx + c$) and quartic ($ax^4 + bx^3 + cx^2 + dx + e$) polynomials. (c) Anharmonicity-induced frequency shift $\omega_{\text{rad}}(\langle n \rangle = 0.5) - \omega_{\text{rad}}(\langle n \rangle = 0)$ as a function of the ground-state trap frequency $\omega_{\text{rad}}(\langle n \rangle = 0)$. The quartic fit, which is a better approximation of a real trapping potential and shows significant frequency shifts, motivates the harmonicity figure of merit introduced in Section 3.2.2. 32

3.3 Ion height d as a function of wafer separation h for the gnd-surface and cross-rf trap geometries, with the surface trap shown as a reference. Both multi-wafer designs show an increasing d with h, as the growing electrode separation pushes the rf-null point further from the substrate. 35

3.4 Harmonicity k, defined from the 2nd-order coefficient of a quadratic fit to a radial electric potential (with $k = 1$ for a perfect quadrupole), as a function of wafer separation h for the gnd-surface and cross-rf traps, with the surface trap shown for reference. A larger k indicates a more harmonic potential, in which the cross-rf trap substantially outperforms both designs, owing to its symmetric electrode geometry, though k decreases with h. The gnd-surface trap improves modestly over the surface trap reference for h greater than the rf–rf electrode spacing, but drops sharply below it at smaller h where wafer proximity breaks the near-quadrupole symmetry. 36

3.5 Trap depth D as a function of wafer separation h for the gnd-surface and cross-rf trap designs, with the surface trap shown as a reference ($D \approx 1$ meV). The logarithmic scale spans nearly three orders of magnitude, highlighting the improvement of both multi-wafer designs over the conventional surface trap. . 37

3.6 (a) Radial trap frequency ω_{rad} as a function of wafer separation h for the multi-wafer trap designs with the surface trap shown for reference. Both multi-wafer designs substantially exceed the surface trap, with frequencies generally increasing at smaller h as the electrode geometry improves harmonicity and reduces r_0. The gnd-surface trap drops sharply when h falls below the rf–rf electrode spacing, consistent with the harmonicity degradation seen in Fig. 3.4. (b) Radial trap frequency as a function of Ω_{rf} at $V_{\mathrm{rf}} = 10\,\mathrm{V}$ for the three trap geometries at fixed $h = 105\,\mu\mathrm{m}$ for the multi-wafer designs. Gray dashed lines indicate constant instability parameter q; the filled points mark the harmonicity-scaled operating q used in (c) ($q = 0.905$ for cross-rf, $q = 0.333$ for gnd-surface, $q = 0.250$ for surface). At equal q, the multi-wafer traps achieve higher ω_{rad}, demonstrating that improved harmonicity directly enables higher trap frequencies for a given drive. (c) Maximum achievable radial frequency at $V_{\mathrm{rf}} = 10\,\mathrm{V}$ as a function of h, using the harmonicity-scaled q from (b). The cross-rf trap achieves a more than $10\times$ improvement over the surface trap (6.12 MHz vs. 1.00 MHz) at $h = 105\,\mu\mathrm{m}$, while the gnd-surface trap peaks at 2.84 MHz when h equals the RF–RF electrode separation. Purple circles in (a) and (c) mark the $h = 105\,\mu\mathrm{m}$ operating point used in Section 3.3. 40

3.7 Motional heating rate $\dot{\bar{n}}$ for the multi-wafer trap designs, normalized to the surface trap heating rate $\dot{\bar{n}}_s$, as a function of wafer separation h. The heating rate is estimated from the empirical scaling $\dot{\bar{n}} \propto \omega_r^{-2} r_0^{-4}$, where the competing dependences on trap frequency and electrode distance are set by each geometry. The cross-rf trap achieves nearly an order of magnitude reduction in heating rate across most of the range studied, while the gnd-surface trap's improvement depends heavily on h. 41

4.1 (a) Photograph of a silicon nitride (Si_3N_4) wafer containing three PICs fabricated in parallel; the device used in this work is highlighted with a blue box. (b) Microscope image of a single dual-ring-assisted Mach-Zehnder modulator (DRMZM), the core optical switching element of the PIC. (c) Microscope image of the input grating coupler array (4×4) and output grating coupler array (1×16), oriented at 90° to each other for polarization-based separation [2]. The 16-channel output array maps directly onto a linear ion chain, with each channel addressing an individual ion site. 48

4.2 (a) Schematic and (b) photograph of the optical setup used to characterize the PIC at 729 nm. The input beam passes through a half-wave plate (HWP) and a quarter-wave plate (QWP) to match the polarization required by the grating couplers. A 2× objective focuses the beam onto the chip surface. Transmitted light is monitored simultaneously by a photodiode for real-time power measurements and a camera for chip imaging, enabling both alignment and coupling efficiency characterization. A flashlight allows for white-light imaging of the chip surface. (c) Photograph of the PIC mounted on a chip carrier with a Thorlabs TECH8 thermoelectric element and AD590 temperature transducer for chip temperature stabilization, used to thermally tune the ring resonators into alignment with the 729 nm laser. The entire assembly is mounted on a three-axis translation stage to achieve precise spatial overlap between the focused input beam and the on-chip grating couplers. 50

GLOSSARY

1D: One dimension

1Q: One-qubit

2Q: Two-qubit

3D: Three dimensions

AOM: Acousto-optic modulator

BE: Boundary element

CMOS: Complementary metal-oxide-semiconductor

dc: Direct current

DRMZM: Dual-ring-assisted Mach–Zehnder modulator

FoM: Figure of merit

FPGA: Field-programmable gate array

HWP: Half-wave plate

MEMS: Microelectromechanical systems

MS: Mølmer–Sørensen

PBS: Polarizing beamsplitter

PCB: Printed circuit board

PDH: Pound–Drever–Hall

PIC: Photonic integrated circuit

PID: Proportional-integral-derivative

PP: Pseudopotential

QHO: Quantum harmonic oscillator

QWP: Quarter-wave plate

rf: Radio-frequency

RWA: Rotating-wave approximation

SPAM: State preparation and measurement

TEC: Thermoelectric cooler

ACKNOWLEDGMENTS

Firstly, I would like to express my deepest gratitude to my research and thesis advisor, Prof. Sara Mouradian, who has been a dedicated and inspiring mentor from my undergraduate years through my first publication and into my master's thesis. Under her guidance and support over the past several years, I have grown tremendously as an engineer, a researcher, and a person.

Subsequently, I extend my heartfelt appreciation to the members of Prof. Mouradian's lab: Rithi Anandwade, Hae Lim, Caleb Walton, and Koray Mentesoglu. It has been a great joy to work alongside such talented colleagues, and I am grateful for their support and for making the past three years such an extraordinary experience.

I would also like to thank Prof. Josh Smith for the opportunity to be part of his Amazon robotics project. This experience not only helped me develop my skills as a researcher but also provided the funding that made this thesis possible. Additionally, I am honored to have Prof. Maxwell Parsons serving on my thesis committee, as much of the theoretical work was shaped by my experience in his Quantum Optics course.

Above all, I would like to thank all the people in my life who have supported me along this journey and will continue to do so in the future. Undoubtedly, I would not be here today without my mother, who is forever my role model of persistence and fearlessness. Lastly, this thesis was completed on the 10th anniversary of the friendships that have been with me through many of life's hardships and successes.

DEDICATION

to my grandfathers, who are now resting on each of my shoulders

Chapter 1
INTRODUCTION

The building blocks of modern digital technology are tiny electronic devices made of semiconductive materials known as *transistors*. Transistors store and manipulate binary information (represented by logical states 0 and 1) by operating in either a conducting ("on") or insulating ("off") state. This binary switching behavior forms the foundation of classical computation. As the number of transistors integrated onto a single chip increases, so too does the amount of information that can be processed and stored, leading directly to improved computational performance. In 1965, Gordon Moore, co-founder of Intel, observed that the number of transistors that could be placed on a chip doubled approximately every year, a trend that is now known as *Moore's law*. Moore's law held for more than half a century as advances in fabrication techniques enabled transistors to shrink to ever smaller dimensions, reaching feature sizes on the order of a few nanometers by 2016 [3, 4]. However, this trend cannot continue indefinitely. As transistor dimensions approach atomic length scales, the assumptions of classical physics begin to break down, and quantum mechanical effects emerge that fundamentally disrupt conventional transistor operation.

Given the apparent limitations imposed by the slowing of Moore's law, one may ask whether computational power will stagnate for the foreseeable future. The answer is no. Throughout history, technological constraints have repeatedly inspired new paradigms, and the impending limits of classical scaling are no exception. The use of quantum mechanical phenomena themselves as the basis for a new computational framework is particularly compelling [5]. Quantum computers offer the potential for *quantum advantage* [6, 7, 8], defined as the ability to solve certain problems intractable for classical computers within any realistic timeframe. This advantage arises from quantum entanglement that allows quantum systems to explore computational spaces in fundamentally different ways from classical machines.

To build quantum hardware capable of enabling computation, a physical platform must

satisfy DiVincenzo's criteria [9], a set of conditions necessary for the realization of a universal quantum computer:

- A scalable physical platform with well-defined qubits.
- The ability to reliably initialize the system to a known state.
- The ability to implement a universal set of quantum logic gates.
- Long coherence times relative to gate operation times.
- The ability to perform qubit-selective measurement.

A wide range of physical platforms have been proposed for quantum computation, including superconducting circuits, trapped ions, neutral atoms, and solid-state defects. Among these, trapped-ion quantum processors have emerged as a particularly promising candidate and currently exhibit some of the lowest error rates for entangling gate operations [10, 11, 12, 13, 14]. In trapped-ion systems, quantum information is encoded in the electronic states of ions confined by electromagnetic fields, while their shared motional modes enable interactions between qubits. These systems have enabled a variety of quantum technologies, including atomic clocks [15], quantum sensors [16], and both analog [17] and digital [18, 19] quantum computers. Qubits encoded in the electronic states of trapped ions benefit from fast and high-fidelity state preparation and measurement (SPAM) [20], as well as high-precision single- and two-qubit operations implemented using either optical [21, 22, 23] or microwave-based [24, 25, 26] gate schemes. Despite these advantages, a central challenge for trapped-ion platforms remains the ability to scale to large numbers of qubits while simultaneously maintaining high-fidelity quantum operations.

This thesis aims to investigate and propose solutions to two key challenges affecting laser-based gate operations in trapped-ion systems: scalable trap geometry and scalable laser delivery. While trap geometry has been the focus of extensive research across the trapped-ion community, there is currently no comprehensive framework for quantitatively assessing the scalability of new trap designs. In this work, such a framework is developed and applied, and a novel scalable trap architecture is proposed that has the potential to further advance the state of the art. In parallel, scalable optical gate delivery is examined. Conventional approaches rely on bulk free-space optics or trap-integrated photonic components. Here, we

introduce an alternative approach based on a separate photonic integrated circuit (PIC), decoupled from the ion trap, that enables flexible and scalable optical control through a field-programmable gate array (FPGA) platform.

Chapter 2 reviews the theoretical foundations of quantum bits, including their representation as two-level electronic states, the quantum harmonic oscillator model, and the physical implementation using $^{40}Ca^{+}$ ions in an oscillating electromagnetic field. It also covers the implementation of single-qubit and entangling gates using laser-driven interactions. Chapter 3 examines the impact of trap geometry on the scalability and fidelity of gate operations. Chapter 4 presents an FPGA-controlled photonic integrated circuit for scalable laser delivery. Finally, Chapter 5 summarizes the results of this research and outlines directions for future work.

Chapter 2

THEORY

2.1 Physical Implementation

This section establishes the foundations for using trapped ions as a platform for quantum computation. We begin by introducing the two-level system that forms the basis of a qubit, with its physical realization given by discrete electronic energy levels of the $^{40}Ca^{+}$ ion. We then describe the principles of ion trapping, including the generation of confining electromagnetic potentials. Finally, we show how the trapping potential, together with the quantized motion of the ion, gives rise to a quantum harmonic oscillator description.

2.1.1 Ions as Qubits

The Two-level System

In this section, we provide a brief overview of the two-level system, which forms the basis for quantum computation. Fig. 2.1a illustrates the *Bloch sphere* [27], which provides a geometric representation of all possible states of a single quantum bit. Here, θ represents the rotation angle of the state $|\psi\rangle$ around the xz-plane while φ is the rotation angle around the xy-plane. In this representation, the logical basis states $|0\rangle$ and $|1\rangle$ correspond to the north and south poles of the sphere along the z-axis, and are eigenstates of the Pauli operator σ_z. More generally, the Pauli matrices define the Cartesian axes of the Bloch sphere, with σ_x, σ_y, and σ_z corresponding to measurements along the x-, y-, and z-directions, respectively. The eigenstates of each Pauli operator are represented by antipodal points on the sphere along the corresponding axis. Appendix A.1 summarizes all the useful mathematical expression of the Pauli matrices.

The set of all possible qubit states spans a complex vector space known as the Hilbert space. For a two-level quantum system, this Hilbert space is two-dimensional. Unlike a classical bit, which can exist only in the states “on” or “off”, a qubit may exist in a coherent

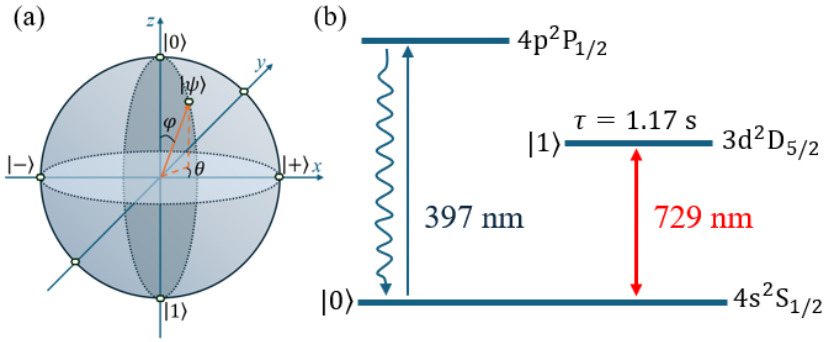

Figure 2.1: (a) The Bloch sphere provides a geometric representation of all possible pure states of a qubit, parameterized by polar angle θ and azimuthal angle φ. The north and south poles correspond to the computational basis states $|0\rangle$ and $|1\rangle$. (b) Relevant energy levels of the $^{40}Ca^{+}$ ion. The qubit is encoded in the $4s^2S_{1/2}$ ground state $|0\rangle$ and the metastable $3d^2D_{5/2}$ state $|1\rangle$, which are coupled by the 729 nm electric quadrupole "clock" transition used for qubit manipulation. The long natural lifetime of the $D_{5/2}$ state ($\tau = 1.17$ s) suppresses spontaneous emission. State-dependent fluorescence on the 397 nm $S_{1/2} \leftrightarrow P_{1/2}$ transition provides qubit readout: an ion in $|0\rangle$ scatters photons ("bright"), while an ion shelved in $|1\rangle$ remains dark.

superposition of the basis states $|0\rangle$ and $|1\rangle$. An arbitrary pure qubit state is written as [27]

$$|\psi\rangle = \cos\left(\frac{\theta}{2}\right)|0\rangle + e^{i\varphi}\sin\left(\frac{\theta}{2}\right)|1\rangle\,. \tag{2.1}$$

Information about the state of a qubit is obtained by measuring physical observables, which are represented in quantum mechanics by Hermitian operators. One of the most important observables is the energy of the system, described by the Hamiltonian operator $\hat{\mathcal{H}}$. The energy eigenstates $|\psi_k\rangle$ satisfy the eigenvalue equation

$$\hat{\mathcal{H}}\,|\psi_k\rangle = E_k\,|\psi_k\rangle\,, \tag{2.2}$$

where E_k is the corresponding energy eigenvalue.

For a time-dependent quantum state $|\psi(t)\rangle$, where t is time, the Hamiltonian governs the

temporal evolution of the system through the time-dependent Schrödinger equation [28],

$$\hat{\mathcal{H}} \left|\psi(t)\right\rangle = i\hbar \frac{d}{dt} \left|\psi(t)\right\rangle . \tag{2.3}$$

This equation describes how quantum states evolve under the influence of the system Hamiltonian. For a time-independent Hamiltonian, the formal solution of Eq. (2.3) can be expressed in terms of the time-evolution operator

$$\hat{U}(t) = \exp\left(-\frac{i}{\hbar}\hat{\mathcal{H}}t\right). \tag{2.4}$$

The quantum state at time t is then given by

$$\left|\psi(t)\right\rangle = \hat{U}(t) \left|\psi(0)\right\rangle . \tag{2.5}$$

Ion of Choice: $^{40}Ca^{+}$ Ion

Ions most commonly used for the physical implementation of quantum information platforms are alkaline-earth metals from Group II of the periodic table [29]. These elements possess two valence electrons; after single ionization, only one valence electron remains, resulting in an atomic structure that closely resembles that of a hydrogen atom. This hydrogen-like structure greatly simplifies both theoretical analysis and experimental control. In this thesis, we focus on the $^{40}\mathrm{Ca}^{+}$ ion.

Owing to its even mass number ($A = 40$), $^{40}\mathrm{Ca}^{+}$ has zero nuclear spin and therefore exhibits no hyperfine structure [29], further simplifying its level structure, as shown in Fig. 2.1b. Calcium atoms are ionized to become $^{40}\mathrm{Ca}^{+}$, which is then subjected to SPAM procedures. We mainly concentrate on the manipulation of a qubit encoded in the atomic transition $4s\,^2\mathrm{S}_{1/2} \leftrightarrow 3d\,^2\mathrm{D}_{5/2}$ of $^{40}\mathrm{Ca}^{+}$. This transition is an electric quadrupole transition at a wavelength of 729 nm and has an exceptionally narrow natural linewidth of $\Gamma/(2\pi) \approx 136$ mHz, corresponding to a metastable lifetime of $\tau \approx 1.168(7)$ s [30]. The long coherence time associated with this metastable excited state is a key advantage of trapped-ion quantum platforms. The 397 nm transition shown in Fig. 2.1b is used for fluorescence-based readout, producing a signal with a probability determined by the population of the $|0\rangle$ state.

In the absence of external driving fields, the atomic Hamiltonian of this two-level system can be written as [27]

$$\hat{\mathcal{H}}_{\text{atom}} = \frac{\hbar\omega_{01}}{2}\sigma_z, \tag{2.6}$$

where ω_{01} is the transition frequency between the qubit states.

2.1.2 Trapping Potential

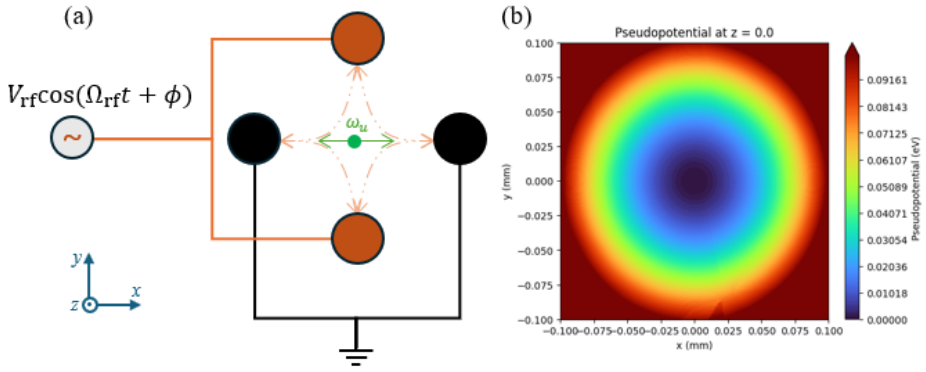

Figure 2.2: (a) The four-rod electrode geometry of a linear Paul trap, where two opposing electrodes are driven by a radio-frequency (rf) source of $V_{\text{rf}}\cos(\Omega_{\text{rf}}t + \phi)$, while the remaining two electrodes are held at ground. The resulting time-dependent quadrupole field creates a net radial confinement when Ω_{rf} is much larger than the ion's motion. In this limit, the micromotion driven at Ω_{rf} averages out and the ion undergoes slow secular harmonic oscillation at frequency ω_r about the RF null at the trap center. (b) Representative radial pseudopotential at the axial midpoint ($z = 0$) of a linear Paul trap similar to (a). The pseudopotential approximation replaces the time-varying field with an effective static potential, valid when $\omega_r \ll \Omega_{\text{rf}}$, and forms a harmonic well for ion confinement.

In 1989, Wolfgang Paul was awarded the Nobel Prize in Physics for the development of the radio-frequency ion trap [31], which enables the confinement of charged particles using oscillating electric fields. In a Paul trap, confinement in two directions, referred to in this thesis as the radial directions, is achieved using a time-dependent radio-frequency (rf) field

(shown in Fig. 2.2a, while confinement along the remaining axial direction is provided by a static (dc) electric potential. The total electric potential inside the trap can be written as:

$$\Phi(x,y,z,t) = \Phi_{\rm dc}(x,y,z) + \Phi_{\rm rf}(x,y,z,t). \tag{2.7}$$

Both components may be expressed as quadrupole fields [32] such that

$$\Phi_{\rm dc}(x,y,z) = \frac{V_{\rm dc}}{2R^2}\left(k_x^{\rm dc}x^2 + k_y^{\rm dc}y^2 + k_z^{\rm dc}z^2\right), \tag{2.8}$$

$$\Phi_{\rm rf}(x,y,z,t) = \frac{V_{\rm rf}}{2R^2}\left(k_x^{\rm rf}x^2 + k_y^{\rm rf}y^2 + k_z^{\rm rf}z^2\right)\cos(\Omega_{\rm rf}t + \phi_{\rm rf}). \tag{2.9}$$

Here, $V_{\rm dc}$ and $V_{\rm rf}$ are the amplitudes of the applied dc and rf voltages, respectively, R is the characteristic trap dimension, $\Omega_{\rm rf}$ is the rf drive angular frequency, and $\phi_{\rm rf}$ is the phase of the rf field. The dimensionless coefficients $k_{x,y,z}^{\rm dc}$ and $k_{x,y,z}^{\rm rf}$ characterize the trap geometry. Since the electric potential satisfies Laplace's equation in free space,

$$\nabla^2\Phi = 0, \tag{2.10}$$

The coefficients obey the constraints $k_x + k_y + k_z = 0$.

The equations of motion for the ion can be separated along each spatial direction. We consider the electric force acting on an ion of mass m and charge e along an arbitrary r-direction where $r = x$, y or z,

$$F_e = m\frac{d^2r}{dt^2} = -e\frac{\partial\Phi}{\partial r}. \tag{2.11}$$

Taking the derivative of the potential in Eq. (2.7) with respect to arbitrary r yields

$$\frac{\partial\Phi}{\partial r} = \frac{r}{R^2}\left(V_{\rm dc}k_r^{\rm dc} + V_{\rm rf}k_r^{\rm rf}\cos(\Omega_{\rm rf}t + \phi_{\rm rf})\right). \tag{2.12}$$

Substituting this (2.12) expression into the Eq. (2.11) gives

$$\frac{d^2r}{dt^2} = -\frac{er}{mR^2}\left(V_{\rm dc}k_r^{\rm dc} + V_{\rm rf}k_r^{\rm rf}\cos(\Omega_{\rm rf}t + \phi_{\rm rf})\right). \tag{2.13}$$

Mathieu Form of the Equation of Motion

The equation of motion can be rewritten in the standard Mathieu form [33],

$$\frac{d^2r}{d\zeta^2} + (a_r - 2q_r\cos 2\zeta)\,r = 0, \tag{2.14}$$

where the dimensionless variable ζ is defined by

$$2\zeta = \Omega_{\rm rf} t + \phi_{\rm rf}. \tag{2.15}$$

Using the relation

$$\frac{d^2r}{dt^2} = \frac{\Omega_{\rm rf}^2}{4}\frac{d^2r}{d\zeta^2},$$

the dimensionless Mathieu stability parameters a_r and q_r, associated with the dc and rf fields respectively, are obtained as

$$a_r = \frac{4eV_{\rm dc}k_r^{\rm dc}}{m\Omega_{\rm rf}^2R^2}, \qquad q_r = -\frac{2eV_{\rm rf}k_r^{\rm rf}}{m\Omega_{\rm rf}^2R^2}. \tag{2.16}$$

For each spatial direction r, the solution of the Mathieu equation (2.14) may be expressed using Floquet theory [33] as

$$u(\zeta) = A\sum_{n=-\infty}^{\infty} C_{2n}\cos[(2n \pm \xi_r)\zeta + B]\,, \tag{2.17}$$

where A and B are constants determined by the initial conditions, C_{2n} are Fourier coefficients, and ξ_r is the characteristic multiplier. Transforming back to the time domain from Eq. 2.15, the corresponding frequency components are given by

$$\omega_{r,n} = \frac{(2n \pm \xi_r)\Omega_{\rm rf}}{2}. \tag{2.18}$$

The fundamental secular frequency in an arbitrary direction u is given by

$$\omega_r = \frac{\xi_r\Omega_{\rm rf}}{2}, \tag{2.19}$$

where, for $|a_r| \ll 1$ and $|q_r| \ll 1$, the characteristic multiplier may be approximated as

$$\xi_r \approx \sqrt{a_r + \frac{q_r^2}{2}}. \tag{2.20}$$

In an ideal linear Paul trap, the dc confinement in the radial directions vanishes, such that $a_x = a_y \approx 0$, while no rf field is applied along the axial direction, implying $q_z = 0$. However, due to electrode imperfections, stray fields, and practical design constraints, these

conditions are generally not perfectly satisfied in experimental implementations. Overall, the fundamental motional frequency in the radial direction is

$$\omega_{x,y} = \frac{q_{x,y}\Omega_{\mathrm{rf}}}{2\sqrt{2}} = -\frac{eV_{\mathrm{rf}}k_{x,y}^{\mathrm{rf}}}{\sqrt{2}m\Omega_{\mathrm{rf}}R^2} \tag{2.21}$$

and in the axial direction is

$$\omega_z = \frac{\sqrt{a_z}\Omega_{\mathrm{rf}}}{2} = \sqrt{\frac{eV_{\mathrm{dc}}k_z^{\mathrm{dc}}}{mR^2}} \tag{2.22}$$

where the second equalities are written in terms of experimentally relevant parameters. $R = r_0$ denotes the distance from the trapped ion to the nearest electrode surface.

Pseudopotential

In a realistic trapping field, the ion trajectory decomposes into a slowly varying secular component $\mathcal{U}$ and a rapidly oscillating micromotion component μ [32], such that

$$r = \mathcal{U} + \mu. \tag{2.23}$$

with (i) $\mu \ll \mathcal{U}$ and (ii) $\dot{\mu} \gg \dot{\mathcal{U}}$. With these assumptions, (2.14) may be approximated as

$$\frac{d^2\mu}{d\zeta^2} = -\left(a_r - 2q_r\cos 2\zeta\right)\mathcal{U}. \tag{2.24}$$

For $a_r \approx 0$, integration yields

$$\mu = -\frac{q_r}{2}\mathcal{U}\cos 2\zeta. \tag{2.25}$$

Substituting Eq. (2.25) into Eq. (2.23), the total trajectory becomes

$$r = \left(1 - \frac{q_r}{2}\cos 2\zeta\right)\mathcal{U}. \tag{2.26}$$

Substituting this expression for r back into Eq. (2.14), we obtain

$$\frac{d^2r}{d\zeta^2} = -\left(a_r - 2q_r\cos 2\zeta\right)\left(1 - \frac{q_r}{2}\cos 2\zeta\right)\mathcal{U}. \tag{2.27}$$

The above analysis provides explicit expressions for the accelerations experienced by an ion in the oscillating electric fields. This result forms the basis for understanding the concept of the pseudopotential, which will be formally defined shortly. To derive the pseudopotential, one must consider the time-averaged acceleration of the ion over one rf drive period.

We first examine the contribution arising from the micromotion component μ. From Eq. (2.24), the micromotion is periodic with the rf frequency. Consequently, its acceleration averages to zero over one rf period

$$\left\langle \frac{d^2\mu}{d\zeta^2} \right\rangle = \frac{1}{\pi}\int_0^\pi \frac{d^2\mu}{d\zeta^2}\, d\zeta = 0. \tag{2.28}$$

Next, we consider the time-averaged acceleration of the secular motion $\mathcal{U}$. Unlike the micromotion, this component does not average to zero over one rf period. Using the same assumptions (i) and (ii) as before, and $\dot{\mu} \gg \dot{\mathcal{U}}$, we can approximate $\ddot{\mathcal{U}} \approx \ddot{r}$. The time-averaged acceleration is then obtained by integrating Eq. (2.27) over one rf period:

$$\left\langle \frac{d^2\mathcal{U}}{d\zeta^2} \right\rangle = \frac{1}{\pi}\int_0^\pi \frac{d^2 r}{d\zeta^2}\, d\zeta = -(a_r + \frac{q_r^2}{2})\mathcal{U} \equiv -\xi_r^2 \mathcal{U}. \tag{2.29}$$

where ξ_r is defined as in Eq. (2.20). Again, switching to real-time scale from Eq. (2.15), the average acceleration of an ion is,

$$\left\langle \frac{d^2\mathcal{U}}{dt^2} \right\rangle = -\frac{\xi_r^2 \Omega_{\mathrm{rf}}^2}{4}\mathcal{U}. \tag{2.30}$$

We can now define the *pseudopotential*, which represents the effective potential generated by the time-averaged acceleration of the secular motion. In one direction r, the pseudopotential D_r is defined such that

$$m\left\langle \frac{d^2\mathcal{U}}{dt^2} \right\rangle = -e\frac{dD_r}{d\mathcal{U}}. \tag{2.31}$$

This relation is analogous to the standard equation of motion for an ion in an electric field, $m\ddot{\mathbf{r}} = -e\nabla\Phi(\mathbf{r})$, where $\Phi(\mathbf{r})$ is the instantaneous electric potential and $\mathbf{r}$ is the ion position vector. Integrating Eq. (2.31) along the arbitrary r-direction yields

$$D_r = \frac{1}{8} V_{\mathrm{rf}} k_r^{\mathrm{rf}} q_r r^2. \tag{2.32}$$

Next, we consider the squared magnitude of the rf electric field gradient,

$$|\nabla\Phi_{\mathrm{rf}}|^2 = \frac{V_{\mathrm{rf}}^2}{R^4}\left[(k_x^{\mathrm{rf}}x)^2 + (k_y^{\mathrm{rf}}y)^2 + (k_z^{\mathrm{rf}}z)^2\right]. \tag{2.33}$$

Using this result, the three-dimensional (3D) pseudopotential can be written in compact form as

$$\mathrm{PP}(x,y,z) = D_x + D_y + D_z = \frac{e^2}{4m\Omega_{\mathrm{rf}}^2}\left|\nabla\Phi_{\mathrm{rf}}(x,y,z)\right|^2. \tag{2.34}$$

$D_z \approx 0$ for the rf field is only creating the pseudopotential in the radial plane. Fig. 2.2b is the time-average potential for a standard linear Paul trap, where the center is the rf-null point of essentially zero potential and the location of an ion.

Quantum Harmonic Oscillator

Ions trapped in electric fields can be optically cooled to the point where their motional energy becomes quantized. This motivates the introduction of the quantum harmonic oscillator (QHO), coherent states, and the operators that act on the motional states of the ions [34]. These concepts are essential for the analysis of qubit gates presented in later sections.

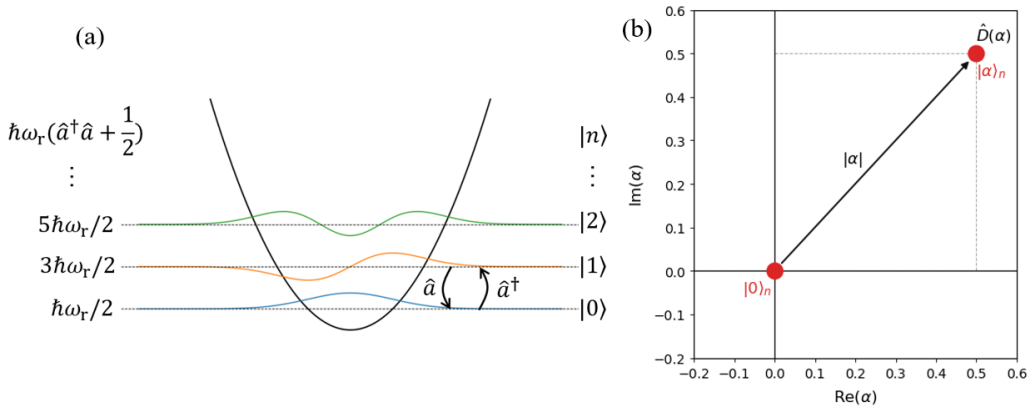

Figure 2.3: (a) Energy level diagram of the quantum harmonic oscillator (QHO) with Hamiltonian $\hat{\mathcal{H}}_{\text{QHO}}$ from (2.40), describing the secular motion of a trapped ion at frequency ω_r. The equally spaced levels $\hbar\omega_r(n+1/2)$ define the Fock states $|n\rangle$, with ladder operators $\hat{a}$ and $\hat{a}^\dagger$ stepping between them. The overlaid wavefunctions $\psi_n(r)$ from (2.44) show the growing spatial extent and node count with n, reflecting increasing positional uncertainty and kinetic energy. (b) Phase-space representation of the displacement operator $\hat{D}(\alpha)$ acting on the motional ground state $|0\rangle_n$. The complex displacement α encodes both the magnitude $|\alpha|$ and direction of the shift, producing a coherent state $|\alpha\rangle_n$ at $(\text{Re}(\alpha), \text{Im}(\alpha)) = (0.5, 0.5)$.

In the quantum description, the ion's position and momentum are represented by the operators $\hat{r}$ and $\hat{p}$. Analogously to the classical case, the total energy of a particle in the

oscillator is given by the sum of its kinetic and potential energies in one direction (1D), yielding the Hamiltonian

$$\hat{\mathcal{H}}_{\mathrm{QHO}} = \frac{\hat{p}^2}{2m} + \frac{1}{2} m\omega_r^2 \hat{r}^2, \tag{2.35}$$

where ω_r is the motional frequency defined in Eq. (2.19).

The harmonic oscillator potential is represented by the quadratic curve shown in Fig. 2.3a. We introduce the annihilation and creation ladder operators, which correspond to the removal or addition of a single phonon,

$$\hat{a} = \frac{1}{\sqrt{2\hbar m\omega_r}} \left(m\omega_r \hat{r} + i\hat{p}\right), \tag{2.36}$$

$$\hat{a}^\dagger = \frac{1}{\sqrt{2\hbar m\omega_r}} \left(m\omega_r \hat{r} - i\hat{p}\right), \tag{2.37}$$

which satisfy the canonical commutation relation $[\hat{a}, \hat{a}^\dagger] = 1$. The position and momentum operators can then be expressed as

$$\hat{r} = \sigma_0\big(\hat{a} + \hat{a}^\dagger\big) \quad \text{and} \quad \hat{p} = \frac{i\hbar}{2\sigma_0}\big(\hat{a}^\dagger - \hat{a}\big), \tag{2.38}$$

where

$$\sigma_0 = \sqrt{\frac{\hbar}{2m\omega_r}} \tag{2.39}$$

is the zero-point spread, i.e., the spatial extent of the ion's wavefunction in its lowest-energy state. Substituting Eq. (2.38) into Eq. (2.35) yields the Hamiltonian in its standard form,

$$\hat{\mathcal{H}}_{\mathrm{QHO}} = \hbar\omega_r \left(\hat{a}^\dagger \hat{a} + \frac{1}{2}\right), \tag{2.40}$$

with ground-state energy $E_0 = \hbar\omega_r/2$.

The number operator $\hat{a}^\dagger\hat{a}$ acts on the Fock (number) states $|n\rangle$ as

$$\hat{a}^\dagger \hat{a} \,|n\rangle = n \,|n\rangle \,. \tag{2.41}$$

The oscillator therefore possesses a discrete ladder of energy eigenstates (Fig. 2.3a), where each Fock state $|n\rangle$ corresponds to a quantized motional excitation (a phonon) with eigenvalue $n \in \mathbb{N}$. The ladder operators raise or lower the motional quantum number by one,

$$\hat{a} \,|n\rangle = \sqrt{n} \;|n-1\rangle \,, \tag{2.42}$$

$$\hat{a}^\dagger \,|n\rangle = \sqrt{n+1} \;|n+1\rangle \,, \tag{2.43}$$

corresponding physically to the removal or addition of a single phonon, respectively. The energy eigenstates have wavefunctions

$$\psi_n(r) = \frac{1}{\sqrt{2^n n!}} \left(\frac{m\omega_r}{\pi\hbar}\right)^{1/4} H_n\left(\sqrt{\frac{m\omega_r}{\hbar}}\, r\right) e^{-\frac{m\omega_r r^2}{2\hbar}}, \tag{2.44}$$

where H_n are the Hermite polynomials. The corresponding probability densities $|\psi_n(r)|^2$, overlaid on the energy levels in Fig. 2.3a, describe the spatial distribution of the ion in the nth motional state, with spatial spread

$$\sigma_n = \sigma_0 \sqrt{(2n+1)}. \tag{2.45}$$

Rather than specifying the exact position of the ion, the wavefunction provides the probability distribution of position measurements.

An important operator associated with the oscillator is the displacement operator demonstrated in Fig. 2.3b,

$$\hat{D}(\alpha) = \exp\left(\alpha\hat{a}^\dagger - \alpha^*\hat{a}\right), \quad \alpha \in \mathbb{C}. \tag{2.46}$$

It generates coherent states from the vacuum,

$$|\alpha\rangle_n = \hat{D}(\alpha)\,|0\rangle_n = \sum_{n=0}^{\infty} e^{-\frac{|\alpha|^2}{2}} \frac{\alpha^n}{\sqrt{n!}}\,|n\rangle = \sum_{n=0}^{\infty} c_n\,|n\rangle\,. \tag{2.47}$$

Using Eq. (2.38), the expectation values of position and momentum in a coherent state are

$$\langle\hat{r}\rangle = \langle\alpha|\,\hat{r}\,|\alpha\rangle = \sigma_0\,\langle\alpha|\,(\hat{a}+\hat{a}^\dagger)\,|\alpha\rangle = 2\sigma_0\,\mathrm{Re}(\alpha), \tag{2.48}$$

$$\langle\hat{p}\rangle = \langle\alpha|\,\hat{p}\,|\alpha\rangle = \frac{i\hbar}{2\sigma_0}\,\langle\alpha|\,(\hat{a}^\dagger-\hat{a})\,|\alpha\rangle = \frac{\hbar}{\sigma_0}\,\mathrm{Im}(\alpha), \tag{2.49}$$

where we used $\hat{a}\,|\alpha\rangle = \alpha\,|\alpha\rangle$. Their variances are therefore

$$(\Delta r)^2 = \langle\hat{r}^2\rangle - \langle\hat{r}\rangle^2 = \sigma_0^2, \tag{2.50}$$

$$(\Delta p)^2 = \langle\hat{p}^2\rangle - \langle\hat{p}\rangle^2 = \frac{\hbar^2}{4\sigma_0^2}. \tag{2.51}$$

Their product

$$\Delta r\,\Delta p = \frac{\hbar}{2}, \tag{2.52}$$

saturates the Heisenberg uncertainty bound,

$$\Delta r\,\Delta p \geq \frac{\hbar}{2}. \tag{2.53}$$

Thus, coherent states are minimum-uncertainty states: they achieve the lowest possible uncertainty product allowed by quantum mechanics and represent the closest quantum analogue to classical oscillatory motion, with $|\alpha|^2 = \bar{n}$ setting the amplitude. The phonon occupation probabilities $P_\alpha(n) = |c_n|^2$ follow a Poisson distribution with mean phonon number $\bar{n} = |\alpha|^2$ and standard deviation $\sqrt{\bar{n}}$.

2.2 Single-qubit (1Q) Gate

In this section, we formulate the dynamics of a trapped ion interacting with an external driving field, providing the foundation for the implementation of optical gates.

Interaction picture

Let $\hat{\mathcal{H}}_{\text{field}}$ denote the Hamiltonian describing the coupling of the ion to an external driving field. The energy associated with this perturbation is given by the expectation value

$$E(t) = \langle\psi(t)|\hat{\mathcal{H}}_{\text{field}}|\psi(t)\rangle, \tag{2.54}$$

where $|\psi(t)\rangle$ is the time-evolved quantum state introduced in Eq. (2.5). For theoretical convenience, it is useful to express the interaction in terms of the initial state $|\psi(0)\rangle$. This is achieved by transforming into the interaction picture, defining the interaction-picture Hamiltonian [28]

$$\hat{\mathcal{H}}_{\text{int}}(t) = \hat{U}^\dagger(t)\,\hat{\mathcal{H}}_{\text{field}}\,\hat{U}(t), \tag{2.55}$$

where $\hat{U}(t)$ describes the unperturbed evolution of the system. This transformation allows the dynamics induced by the driving field to be treated relative to the natural evolution of the ion.

Logic gates in trapped-ion systems are implemented using an electromagnetic field with drive frequency ω_d. A monochromatic plane-wave solution of the wave equation is

$$\mathbf{E}(\mathbf{r}, t) = \mathbf{E}_0 \cos(\omega_d t - \mathbf{K}\cdot\mathbf{r} + \phi_o)\,, \tag{2.56}$$

where

- $\mathbf{E}_0 = E_0\hat{\boldsymbol{\epsilon}}$ is the electric-field amplitude with polarization unit vector $\hat{\boldsymbol{\epsilon}} = (\epsilon_x, \epsilon_y, \epsilon_z)$,

- $\mathbf{K} = (K_x, K_y, K_z)$ is the wave vector with magnitude $K = |\mathbf{K}| = \omega_d/c = 2\pi/\lambda$,
- $\mathbf{r} = (x, y, z)$ is the position vector of the ion, and
- ϕ_o is the optical phase offset of the laser relative to the qubit reference frame.

We restrict the internal dynamics of the ion to an effective two-level system spanned by the states $|0\rangle$ and $|1\rangle$. The interaction with the driving field takes the form [18, 35]

$$\hat{\mathcal{H}}_{\text{field}} = -\mathbf{Q} \cdot \mathbf{E}(\mathbf{r}, t), \tag{2.57}$$

where $\mathbf{Q}$ represents the effective quadrupole coupling of the ion to the electric field. The strength of this interaction is characterised by the Rabi frequency

$$\hbar\Omega = |\mathbf{Q} \cdot \mathbf{E}_0| \propto E_0\sqrt{\Gamma}. \tag{2.58}$$

The Rabi frequency Ω, which sets the transition rate between the two energy levels, is proportional to the driving-field amplitude E_0 and to the square root of the natural linewidth Γ. For a long-lifetime qubit such as the $^{40}Ca^+$ ion, Γ is small (Section 2.1.1). This hierarchy of timescales will be exploited in the rotating wave approximation (RWA) introduced below.

Since the driving field induces transitions between $|0\rangle$ and $|1\rangle$, the interaction Hamiltonian can be written in terms of the Pauli operator $\hat{\sigma}_x$,

$$\hat{\mathcal{H}}_{\text{field}} = -\hbar\Omega\hat{\sigma}_x \cos(\omega_d t - \mathbf{K} \cdot \mathbf{r} + \phi_o). \tag{2.59}$$

Electronic interaction picture We first transform into the interaction picture defined by the atomic Hamiltonian from Eq. (2.6). The corresponding unitary transformation is

$$\hat{U}_{\text{atom}}(t) = e^{-\frac{i}{\hbar}\hat{\mathcal{H}}_{\text{atom}}t} = e^{-i\omega_{01}t\hat{\sigma}_z/2}. \tag{2.60}$$

Applying this transformation gives the interaction Hamiltonian

$$\hat{\mathcal{H}}^{\text{atom}}_{\text{int}}(t) = \hat{U}^{\dagger}_{\text{atom}}(t)\hat{\mathcal{H}}_{\text{field}}\hat{U}_{\text{atom}}(t) \tag{2.61}$$

$$= -\hbar\Omega\left(\hat{\sigma}_x \cos\omega_{01}t - \hat{\sigma}_y \sin\omega_{01}t\right)\cos(\omega_d t - \mathbf{K} \cdot \mathbf{r} + \phi_o). \tag{2.62}$$

Next, we consider the quantized motion of the trapped ion. Restricting the motion to a single direction r, the spatial phase becomes

$$\mathbf{K} \cdot \mathbf{r} = K_r\hat{r}. \tag{2.63}$$

Introducing the Lamb–Dicke parameter $\eta = K_r\sigma_0$, where σ_0 is the ground function spread from (2.39). Plugging the position operator from Eq. (2.38), we can write

$$\mathbf{K}\cdot\mathbf{r} = \eta(\hat{a}^\dagger + \hat{a}). \tag{2.64}$$

Using Euler's formula, $\cos\theta = \frac{1}{2}(e^{i\theta} + e^{-i\theta})$, the field term becomes

$$\cos(\omega_d t - \mathbf{K}\cdot\mathbf{r}) = \frac{1}{2}\left[e^{i(\omega_d t+\phi_o)}e^{-i\eta(\hat{a}^\dagger+\hat{a})} + e^{-i(\omega_d t+\phi_o)}e^{i\eta(\hat{a}^\dagger+\hat{a})}\right]. \tag{2.65}$$

In the Lamb–Dicke regime ($\eta \ll 1$), the exponentials can be expanded to first order,

$$e^{\pm i\eta(\hat{a}^\dagger+\hat{a})} \approx 1 \pm i\eta(\hat{a}^\dagger + \hat{a}). \tag{2.66}$$

Substituting this expansion gives

$$\hat{\mathcal{H}}_{\text{field}} = -\frac{\hbar\Omega}{2}\hat{\sigma}_x\Big[e^{i(\omega_d t+\phi_o)} + e^{-i(\omega_d t+\phi_o)} - e^{i(\omega_d t+\phi_o)}(\hat{a}^\dagger+\hat{a}) + e^{-i(\omega_d t+\phi_o)}(\hat{a}^\dagger+\hat{a})\Big]. \tag{2.67}$$

Motional interaction picture The QHO time-evolution operator given the Hamiltonian from Eq. (2.40) is

$$\hat{U}_{\text{QHO}}(t) = e^{-\frac{i}{\hbar}\hat{\mathcal{H}}_{\text{QHO}}t} = e^{-i\omega_r t(\hat{a}^\dagger\hat{a}+1/2)}. \tag{2.68}$$

Transforming into this interaction picture yields

$$\begin{aligned}\hat{\mathcal{H}}_{\text{int}}(t) = &-\frac{\hbar\Omega}{2}\left(\hat{\sigma}_x\cos\omega_{01}t - \hat{\sigma}_y\sin\omega_{01}t\right)\\ &\cdot\Big[e^{i(\omega_d t+\phi_o)} - i\eta e^{i(\omega_d t+\phi_o)}\left(e^{+i\omega_u t}\hat{a}^\dagger + e^{-i\omega_u t}\hat{a}\right) + \text{h.c.}\Big].\end{aligned} \tag{2.69}$$

Complete interaction picture It is convenient to express the Hamiltonian using the raising and lowering operators $\hat{\sigma}_\pm$. Using the identity from Eq. (A.21), the interaction Hamiltonian becomes

$$\begin{aligned}\hat{\mathcal{H}}_{\text{int}} = &-\frac{\hbar\Omega}{2}\left(e^{i\omega_{01}t}\hat{\sigma}_+ + e^{-i\omega_{01}t}\hat{\sigma}_-\right)\\ &\cdot\Big[e^{i(\omega_d t+\phi_o)} - i\eta e^{i(\omega_d t+\phi_o)}\left(e^{+i\omega_u t}\hat{a}^\dagger + e^{-i\omega_u t}\hat{a}\right) + \text{h.c.}\Big].\end{aligned} \tag{2.70}$$

Now, defining the laser drive frequency detuning from the qubit transition frequency as $\delta = \omega_d - \omega_{01}$, we expand Eq. (2.70) and collect oscillating terms by multiplying the Pauli

operators through the full bracket of Eq. (2.70), including the hermitian conjugate explicitly. This yields two frequency contributions: terms oscillating at $\pm(\omega_d - \omega_{01}) = \pm\delta$, and terms oscillating at $\pm(\omega_d + \omega_{01})$. Since the laser operates near-resonantly, $\omega_d \simeq \omega_{01}$, the latter satisfy $\omega_d + \omega_{01} \simeq 2\omega_{01} \gg \Omega$, meaning they oscillate far more rapidly than the driven dynamics and are discarded under the RWA. The surviving interaction Hamiltonian is therefore

$$\begin{aligned}\hat{\mathcal{H}}_{\text{int}}(t) \simeq -\frac{\hbar\Omega}{2}\Big\{ & e^{-i\phi_o}\hat{\sigma}_+\Big[e^{-i\delta t} + i\eta e^{-i\delta t}\left(e^{-i\omega_r t}\hat{a} + e^{+i\omega_r t}\hat{a}^\dagger\right)\Big] \\ & + e^{+i\phi_o}\hat{\sigma}_-\Big[e^{+i\delta t} - i\eta e^{+i\delta t}\left(e^{-i\omega_r t}\hat{a} + e^{+i\omega_r t}\hat{a}^\dagger\right)\Big]\Big\}.\end{aligned} \tag{2.71}$$

Carrier transition

For single-qubit rotations on the carrier transition, the laser drive frequency is resonant with the electronic transition frequency ($\omega_d = \omega_{01}$, i.e. $\delta = 0$). Within the Lamb–Dicke regime, where the ion's motional excursion is much smaller than the laser wavelength, we further require $\Omega \ll \omega_u$, meaning the Rabi frequency is far below the trap frequency. This ensures that the RWA is valid, allowing the rapidly oscillating terms at $\pm\omega_u$. With the initial laser phase $\phi_0 = 0$, the Hamiltonian of Eq. (2.71) reduces to

$$\hat{H}_{\text{carrier}} \approx -\frac{\hbar\Omega'}{2}\,\hat{\sigma}_x, \tag{2.72}$$

where the effective Rabi frequency $\Omega' = 2\Omega$. The corresponding time-evolution operator is

$$\hat{U}_{\text{carrier}}(t) = e^{-i\hat{H}_{\text{carrier}}t/\hbar} = e^{i\frac{\Omega' t}{2}\hat{\sigma}_x}. \tag{2.73}$$

For an ion initially prepared in $|0\rangle$, the state evolves as

$$|\psi(t)\rangle = \cos\left(\frac{\Omega' t}{2}\right)|0\rangle + i\sin\left(\frac{\Omega' t}{2}\right)|1\rangle\,. \tag{2.74}$$

The probability of finding the ion in the excited state $|1\rangle$ is therefore

$$P_1(t) = \sin^2\left(\frac{\Omega' t}{2}\right). \tag{2.75}$$

A complete population transfer (a π-pulse) occurs when

$$\Omega' t_\pi = \pi \qquad \Rightarrow \qquad t_\pi = \frac{\pi}{\Omega'}. \tag{2.76}$$

Similarly, a $\pi/2$ pulse that prepares the equal superposition state has duration

$$t_{\pi/2} = \frac{\pi}{2\Omega'}. \tag{2.77}$$

2.3 Two-qubit (2Q) Gate

While single-qubit rotations enable control of individual qubits, universal quantum computation additionally requires the ability to generate entanglement between qubits. In trapped-ion systems, this is commonly achieved through the Mølmer–Sørensen (MS) gate [36, 37], which couples the internal electronic states of multiple ions via their shared collective motional modes, acting as a quantum bus. The gate employs a bichromatic laser field whose two frequency components are symmetrically detuned from the carrier transition, located near the red and blue motional sidebands of a collective vibrational mode, thereby driving a state-dependent force that displaces the shared motional mode along a trajectory in phase space. When the gate time is chosen such that this trajectory closes exactly, the motion disentangles from the qubit register, leaving behind an effective spin–spin interaction that generates entanglement between the ions.

Consider ions confined in the same trapping potential and interacting with a bichromatic laser field that is symmetrically detuned from the motional sidebands by a small amount $\Delta \ll \omega_u$, where ω_u is the frequency of the collective vibrational mode. The applied field contains two frequency components

$$\omega_d = \omega_{01} \pm (\omega_r + \Delta), \tag{2.78}$$

which simultaneously drive the red and blue motional sidebands, corresponding to detunings

$$\delta_{\mathrm{rsb}} = -(\omega_r + \Delta), \qquad \delta_{\mathrm{bsb}} = +(\omega_r + \Delta). \tag{2.79}$$

Red Sideband Substituting $\delta = \delta_{\mathrm{rsb}} = -(\omega_r + \Delta)$ into Eq. 2.71 gives $e^{-i\delta t} = e^{+i(\omega_r+\Delta)t}$. The motional terms in the $\hat{\sigma}_+$ bracket then oscillate at $+\Delta$ for $\hat{a}$ and $+(2\omega_r + \Delta)$ for $\hat{a}^\dagger$, and symmetrically for $\hat{\sigma}_-$. Applying the rotating-wave approximation under $\Delta \ll \omega_r$, all terms oscillating at $\pm(\omega_r + \Delta)$ and $\pm(2\omega_r + \Delta)$ are dropped. The surviving near-resonant terms are $\hat{\sigma}_+\hat{a}\, e^{+i\Delta t}$ and $\hat{\sigma}_-\hat{a}^\dagger e^{-i\Delta t}$, yielding the red-sideband Hamiltonian

$$\hat{\mathcal{H}}_{\mathrm{rsb}} \approx -\frac{i\eta\hbar\Omega}{2}\left(\hat{\sigma}_+\hat{a}\, e^{+i(\Delta t - \phi_{\mathrm{rsb}})} - \hat{\sigma}_-\hat{a}^\dagger e^{-i(\Delta t - \phi_{\mathrm{rsb}})}\right). \tag{2.80}$$

Acting explicitly on the joint spin-motion states $|0,n\rangle$ and $|1,n-1\rangle$,

$$\hat{\mathcal{H}}_{\mathrm{rsb}}\,|0,n\rangle = -\frac{i\eta\hbar\Omega}{2}\sqrt{n}\,e^{+i(\Delta t-\phi_{\mathrm{rsb}})}\,|1,n-1\rangle = \hbar\Omega_{\mathrm{rsb}}\,|1,n-1\rangle\,, \tag{2.81}$$

$$\hat{\mathcal{H}}_{\mathrm{rsb}}\,|1,n-1\rangle = +\frac{i\eta\hbar\Omega}{2}\sqrt{n}\,e^{-i(\Delta t-\phi_{\mathrm{rsb}})}\,|0,n\rangle = \hbar\Omega^{*}_{\mathrm{rsb}}\,|0,n\rangle\,. \tag{2.82}$$

where the time- and phase-dependent red-sideband Rabi frequency is,

$$\Omega_{\mathrm{rsb}} = -\frac{i\eta\Omega\sqrt{n}}{2}e^{+i(\Delta t-\phi_{\mathrm{rsb}})} \tag{2.83}$$

Blue Sideband Substituting $\delta = \delta_{\mathrm{bsb}} = +(\omega_r + \Delta)$ gives $e^{-i\delta t} = e^{-i(\omega_u+\Delta)t}$. By the same RWA argument as before, the surviving near-resonant terms are $\hat{\sigma}_+\hat{a}^\dagger e^{-i\Delta t}$ and $\hat{\sigma}_-\hat{a}\,e^{+i\Delta t}$, yielding the blue-sideband Hamiltonian

$$\hat{\mathcal{H}}_{\mathrm{bsb}} \approx -\frac{i\eta\hbar\Omega}{2}\left(\hat{\sigma}_+\hat{a}^\dagger e^{-i(\Delta t+\phi_{\mathrm{bsb}})} - \hat{\sigma}_-\hat{a}\,e^{+i(\Delta t+\phi_{\mathrm{bsb}})}\right). \tag{2.84}$$

Acting explicitly on $|0,n\rangle$ and $|1,n+1\rangle$,

$$\hat{\mathcal{H}}_{\mathrm{bsb}}\,|0,n\rangle = \frac{i\eta\hbar\Omega}{2}\sqrt{n+1}\,e^{-i(\Delta t+\phi_{\mathrm{bsb}})}\,|1,n+1\rangle = \hbar\Omega_{\mathrm{bsb}}\,|1,n+1\rangle\,, \tag{2.85}$$

$$\hat{\mathcal{H}}_{\mathrm{bsb}}\,|1,n+1\rangle = +\frac{i\eta\hbar\Omega}{2}\sqrt{n+1}\,e^{+i(\Delta t+\phi_{\mathrm{bsb}})}\,|0,n\rangle = \hbar\Omega^{*}_{\mathrm{bsb}}\,|0,n\rangle\,. \tag{2.86}$$

where, again the phase- and time-dependent blue-sideband Rabi frequency is,

$$\Omega_{\mathrm{bsb}} = \frac{i\eta\Omega\sqrt{n+1}}{2}e^{-i(\Delta t+\phi_{\mathrm{bsb}})} \tag{2.87}$$

The sideband Hamiltonians Eqs. (2.80) and (2.84) reveal the fundamental mechanism by which spin and motional degrees of freedom become entangled. In both cases the coupling strength is set not by the bare Rabi frequency Ω, but by the sideband Rabi frequencies Ω_{rsb} (2.83) and Ω_{bsb} (2.87). On the red sideband, the ion can only be excited if $n \geq 1$, since $\hat{a}\,|0\rangle_n = 0$; the process simultaneously flips the qubit $|0\rangle \to |1\rangle$ and removes one phonon. On the blue sideband, no such restriction applies: excitation is possible from any Fock state, and each transition adds one phonon. These two complementary processes form the basis of entangling gates. As illustrated in Fig. 2.4a, the combination of both sidebands on two ions, for example, opens four spin-motion coupling paths from the initial state $|00,n\rangle$. The key feature of the MS gate is that while these paths generate spin-motion entanglement during the gate, the motional mode is fully disentangled from the qubit register at the gate time, leaving behind a purely electronic entangled state.

2.3.1 Mølmer–Sørensen Hamiltonian

To implement the MS gate, the red- and blue-sideband beams co-propagate with equal and opposite detunings Δ. We introduce the spin phase and motional phase

$$\phi_{\text{spin}} = \frac{\phi_{\text{bsb}} + \phi_{\text{rsb}}}{2}, \qquad \phi_{\text{motion}} = \frac{\phi_{\text{bsb}} - \phi_{\text{rsb}}}{2}, \tag{2.88}$$

so that $\phi_{\text{bsb}} = \phi_{\text{spin}} + \phi_{\text{motion}}$ and $\phi_{\text{rsb}} = \phi_{\text{spin}} - \phi_{\text{motion}}$.

In a chain of N ions there are N collective motional modes with frequencies $\omega_{r,j}$ for $j = 1, \ldots, N$. Each mode is characterised by its normal-mode transformation matrix b_{ij}, where the component b_{ij} describes the participation of ion i in mode j, and satisfies the orthonormality relations

$$\sum_{i=1}^{N} b_{ij}\, b_{ik} = \delta_{jk} \qquad \text{and} \qquad \sum_{j=1}^{N} b_{ij}\, b_{kj} = \delta_{ik}. \tag{2.89}$$

The Lamb–Dicke parameter coupling ion i to mode j is

$$\eta_{ij} = b_{ij}\, K_r\, \sigma_{0,j} = b_{ij}\, K_r \sqrt{\frac{\hbar}{2m\omega_{r,j}}}, \tag{2.90}$$

where K_r is the laser wave-vector projection along the direction of motion and m is the ion mass. The bichromatic field simultaneously drives all modes, with detuning from mode j given by

$$\Delta_j = \omega_d - \omega_{01} - \omega_{r,j}. \tag{2.91}$$

Summing Eqs. (2.80) and (2.84) over all ions i and modes j, and substituting $\phi_{\text{rsb}} = \phi_{\text{spin}} - \phi_{\text{motion}}$ and $\phi_{\text{bsb}} = \phi_{\text{spin}} + \phi_{\text{motion}}$,

$$\begin{aligned}
\hat{\mathcal{H}}_{\text{MS}}(t) &= \sum_{i=1}^{N} \left(\hat{\mathcal{H}}_{\text{rsb}}^{(i)} + \hat{\mathcal{H}}_{\text{bsb}}^{(i)} \right) \\
&= -\frac{i\hbar}{2} \sum_{i,j} \Omega_i \eta_{ij} \Big[\hat{\sigma}_+^{(i)} e^{-i\phi_{\text{spin}}} \left(\hat{a}_j e^{i(\Delta_j t + \phi_{\text{motion}})} + \hat{a}_j^\dagger e^{-i(\Delta_j t + \phi_{\text{motion}})} \right) \\
&\qquad\qquad - \hat{\sigma}_-^{(i)} e^{+i\phi_{\text{spin}}} \left(\hat{a}_j e^{i(\Delta_j t + \phi_{\text{motion}})} + \hat{a}_j^\dagger e^{-i(\Delta_j t + \phi_{\text{motion}})} \right) \Big] \\
&= -\frac{i\hbar}{2} \sum_{i,j} \Omega_i \eta_{ij} \left(\hat{\sigma}_+^{(i)} e^{-i\phi_{\text{spin}}} - \hat{\sigma}_-^{(i)} e^{+i\phi_{\text{spin}}} \right) \\
&\qquad\qquad \cdot \left(\hat{a}_j e^{i(\Delta_j t + \phi_{\text{motion}})} + \hat{a}_j^\dagger e^{-i(\Delta_j t + \phi_{\text{motion}})} \right).
\end{aligned} \tag{2.92}$$

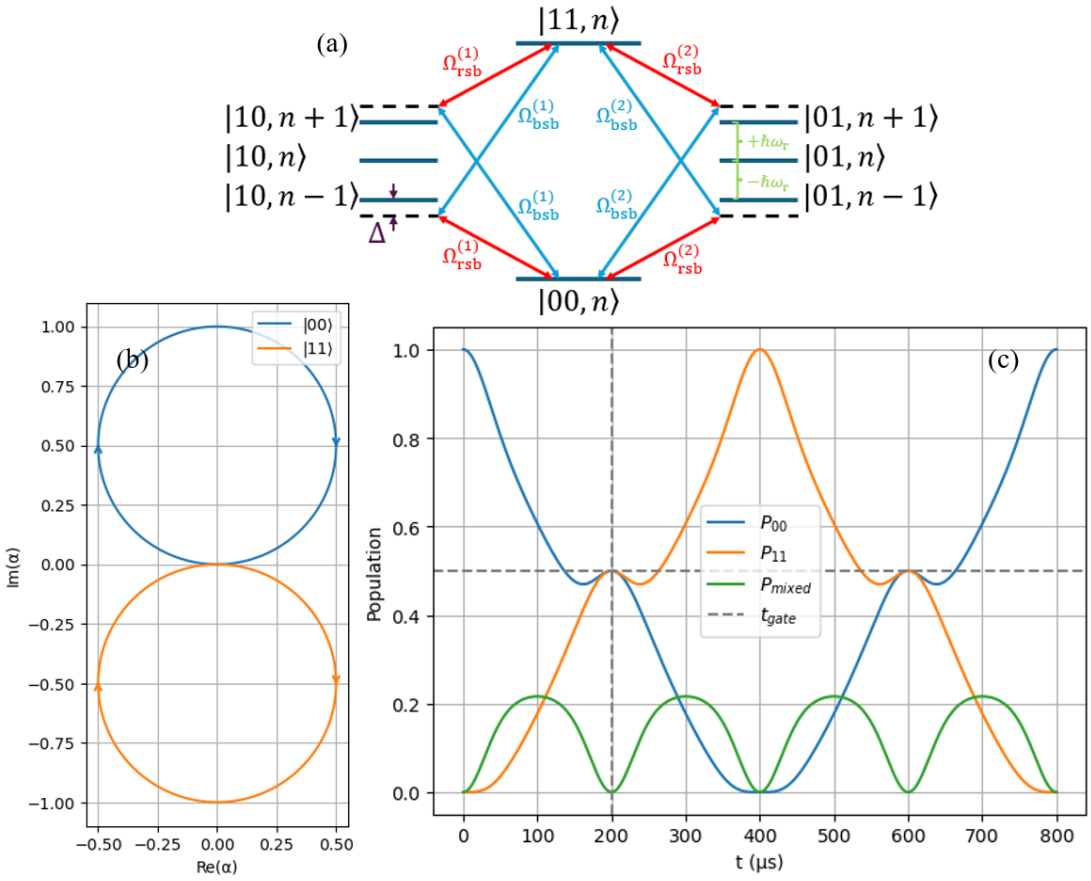

Figure 2.4: (a) Spin-motion energy level diagram of the Mølmer-Sørensen (MS) interaction. Each ion is simultaneously driven by two lasers, one on the blue sideband ($\Omega_{\text{bsb}}^{(1,2)}$) and the other on the red sideband ($\Omega_{\text{rsb}}^{(1,2)}$), each detuned by Δ from the motional sideband frequency. The four resulting coupling paths interfere constructively to entangle the two-qubit spin states while leaving the net motional state unchanged. (b) Phase-space trajectories of the spin-dependent displacement from (2.119). The $|00\rangle$ and $|11\rangle$ spin components trace closed circular orbits of equal radius but opposite orientation, each accumulating a geometric phase proportional to the enclosed area. Loop closure at $\alpha(T) = 0$ guarantees the motional mode disentangles from the qubit register at the gate time. (c) Population dynamics under the MS interaction, initialized in $|00\rangle$. The populations P_{00} and P_{11} undergo coherent oscillation and at t_{gate} (2.121), $P_{00} = P_{11} = 0.5$ and $P_{\text{mixed}} = 0$, indicating the target maximally entangled Bell state has been prepared.

The spin bracket can be decomposed using $\hat{\sigma}_\pm = (\hat{\sigma}_x \pm i\hat{\sigma}_y)/2$, giving

$$\hat{\sigma}_+^{(i)} e^{-i\phi_{\text{spin}}} - \hat{\sigma}_-^{(i)} e^{+i\phi_{\text{spin}}} = i\Big(\cos\phi_{\text{spin}}\,\hat{\sigma}_y^{(i)} - \sin\phi_{\text{spin}}\,\hat{\sigma}_x^{(i)}\Big), \tag{2.93}$$

which yields the general MS Hamiltonian

$$\hat{\mathcal{H}}_{\text{MS}}(t) = \frac{\hbar}{2}\sum_{i=1}^{N}\sum_{j=1}^{N}\Omega_i\eta_{ij}\Big(\cos\phi_{\text{spin}}\,\hat{\sigma}_y^{(i)} - \sin\phi_{\text{spin}}\,\hat{\sigma}_x^{(i)}\Big) \cdot\Big(\hat{a}_j e^{i(\Delta_j t+\phi_{\text{motion}})} + \hat{a}_j^\dagger e^{-i(\Delta_j t+\phi_{\text{motion}})}\Big). \tag{2.94}$$

Equation (2.94) shows that the spin axis of the state-dependent force is controlled by ϕ_{spin}, while ϕ_{motion} sets the quadrature of the motional displacement.

We now apply the phase condition $\phi_{\text{rsb}} = 0$ and $\phi_{\text{bsb}} = \pi$, which gives $\phi_{\text{spin}} = \pi/2$ and $\phi_{\text{motion}} = \pi/2$. Substituting $\cos(\pi/2) = 0$, $\sin(\pi/2) = 1$, and $e^{\pm i\pi/2} = \pm i$, Eq. (2.94) reduces to

$$\begin{aligned}\hat{\mathcal{H}}_{\text{MS}}(t) &= \frac{\hbar}{2}\sum_{i,j}\Omega_i\eta_{ij}\,(-\hat{\sigma}_x^{(i)})\Big(i\hat{a}_j e^{i\Delta_j t} - i\hat{a}_j^\dagger e^{-i\Delta_j t}\Big)\\ &= \frac{i\hbar}{2}\sum_{i,j}\Omega_i\eta_{ij}\,\hat{\sigma}_x^{(i)}\Big(\hat{a}_j^\dagger e^{-i\Delta_j t} - \hat{a}_j e^{+i\Delta_j t}\Big),\end{aligned} \tag{2.95}$$

yielding the standard MS Hamiltonian

$$\hat{\mathcal{H}}_{\text{MS}}(t) = \frac{i\hbar}{2}\sum_{i=1}^{N}\sum_{j=1}^{N}\Omega_i\eta_{ij}\,\hat{\sigma}_x^{(i)}\Big(\hat{a}_j^\dagger e^{-i\Delta_j t} - \hat{a}_j e^{+i\Delta_j t}\Big), \tag{2.96}$$

where each term describes a state-dependent displacement of mode j conditioned on the spin state of ion i along $\hat{\sigma}_x$, with coupling strength set by η_{ij} and Ω_i.

2.3.2 Time Evolution via the Magnus Expansion

A central challenge in time-dependent quantum mechanics is computing the propagator $\hat{U}(t)$ generated by a Hamiltonian $\hat{\mathcal{H}}(t)$ that does not commute with itself at different times,

$$[\hat{\mathcal{H}}(t_1),\,\hat{\mathcal{H}}(t_2)] \neq 0 \quad \text{for } t_1 \neq t_2. \tag{2.97}$$

In such cases, the exponentiation of (2.4) fails because it implicitly assumes commutativity. The *Magnus expansion* [38] resolves this by writing the exact propagator as a single matrix

exponential,

$$\hat{U}(t) = e^{\hat{M}(t)}, \tag{2.98}$$

where $\hat{M}(t) = \sum_{n=1}^{\infty} \hat{M}_n(t)$ is an anti-Hermitian operator, $\hat{M}^\dagger(t) = -\hat{M}(t)$, constructed as a series of nested commutator integrals. Because $\hat{M}(t)$ is anti-Hermitian at every truncation order, $\hat{U}^\dagger(t)\hat{U}(t) = e^{-\hat{M}(t)}e^{\hat{M}(t)} = \hat{I}$ is guaranteed to be unitary. The first three terms are

$$\hat{M}_1(t) = \frac{-i}{\hbar}\int_0^t dt_1\, \hat{\mathcal{H}}(t_1), \tag{2.99}$$

$$\hat{M}_2(t) = \frac{-1}{2\hbar^2}\int_0^t dt_1 \int_0^{t_1} dt_2\, \big[\hat{\mathcal{H}}(t_1),\, \hat{\mathcal{H}}(t_2)\big], \tag{2.100}$$

$$\hat{M}_3(t) = \frac{i}{6\hbar^3}\int_0^t dt_1 \int_0^{t_1} dt_2 \int_0^{t_2} dt_3 \cdot \Big(\big[\hat{\mathcal{H}}(t_1), \big[\hat{\mathcal{H}}(t_2), \hat{\mathcal{H}}(t_3)\big]\big] + \big[\hat{\mathcal{H}}(t_3), \big[\hat{\mathcal{H}}(t_2), \hat{\mathcal{H}}(t_1)\big]\big]\Big). \tag{2.101}$$

Physically, $\hat{M}_1$ is the time-averaged generator-the answer one would obtain if all infinitesimal rotations commuted. $\hat{M}_2$ is the first correction, encoding the total accumulated error from ignoring the ordering of those rotations. Higher orders correct the corrections, each one burying the previous inside a deeper commutator bracket.

First Magnus term. Inserting (2.96) into (2.99) and performing the integral,

$$\hat{M}_1(t) = \sum_{i=1}^{N}\sum_{j=1}^{N} \hat{\sigma}_x^{(i)}\Big(\alpha_{ij}(t)\,\hat{a}^{\dagger(j)} - \alpha_{ij}^*(t)\,\hat{a}^{(j)}\Big), \tag{2.102}$$

where the complex displacement amplitude is

$$\alpha_{ij}(t) = i\frac{\eta_{ij}\Omega_i}{2\Delta_j}\big(e^{-i\Delta_j t} - 1\big)\,, \tag{2.103}$$

with magnitude

$$|\alpha_{ij}(t)| = \frac{\eta_{ij}\Omega_i}{\Delta_j}\left|\sin\!\left(\frac{\Delta_j t}{2}\right)\right|. \tag{2.104}$$

The operator in (2.102) is the generator of a coherent displacement of mode j conditioned on the spin state of the ion i. conditioned on the spin state of ion i. As shown in Fig. 2.4b, each spin component traces a circular arc of radius $\eta_{ij}\Omega_i/2\Delta_j$ in phase space, with the trajectory originating at the vacuum state $|0\rangle_n$ at the origin. The spin-dependent nature of the displacement means that different spin eigenstates are displaced along distinct trajectories, generating entanglement between the spin and motional degrees of freedom during the gate.

Second Magnus term. The commutator of $\hat{\mathcal{H}}_{\mathrm{MS}}(t_1)$ and $\hat{\mathcal{H}}_{\mathrm{MS}}(t_2)$ is

$$\big[\hat{\mathcal{H}}_{\mathrm{MS}}(t_1),\,\hat{\mathcal{H}}_{\mathrm{MS}}(t_2)\big] = -\frac{\hbar^2}{4}\sum_{i=1}^{N}\sum_{k=1}^{N}\sum_{j=1}^{N}\Omega_i\eta_{ij}\,\Omega_k\eta_{kj}\,\hat{\sigma}_x^{(i)}\hat{\sigma}_x^{(k)} \cdot\Big[\hat{a}_j^{\dagger}e^{-i\Delta_j t_1}-\hat{a}_j e^{+i\Delta_j t_1},\;\hat{a}_j^{\dagger}e^{-i\Delta_j t_2}-\hat{a}_j e^{+i\Delta_j t_2}\Big]. \tag{2.105}$$

Using $[\hat{a}_j,\hat{a}_j^{\dagger}]=1$, the bosonic commutator reduces to a pure scalar,

$$\Big[\hat{a}_j^{\dagger}e^{-i\Delta_j t_1}-\hat{a}_j e^{+i\Delta_j t_1},\;\hat{a}_j^{\dagger}e^{-i\Delta_j t_2}-\hat{a}_j e^{+i\Delta_j t_2}\Big] = -2i\sin\big(\Delta_j(t_1-t_2)\big). \tag{2.106}$$

Substituting back, we obtain

$$\big[\hat{\mathcal{H}}_{\mathrm{MS}}(t_1),\,\hat{\mathcal{H}}_{\mathrm{MS}}(t_2)\big] = \frac{i\hbar^2}{2}\sum_{j=1}^{N}\sin\big[\Delta_j(t_1-t_2)\big]\sum_{i=1}^{N}\sum_{k=1}^{N}\Omega_i\eta_{ij}\,\Omega_k\eta_{kj}\,\hat{\sigma}_x^{(i)}\hat{\sigma}_x^{(k)}. \tag{2.107}$$

It is natural at this point to introduce the collective spin operator

$$\hat{S}_x \equiv \sum_{i=1}^{N}\hat{\sigma}_x^{(i)}, \tag{2.108}$$

which will appear explicitly once we specialise to uniform couplings. For now, the coupling weights $\Omega_i\eta_{ij}$ remain explicit. Since the commutator (2.107) is proportional to products of $\hat{\sigma}_x$ operators — which all commute with one another — all higher-order Magnus terms vanish identically. Substituting (2.107) into the second-order Magnus term

$$\hat{M}_2(t) = \frac{-1}{2\hbar^2}\int_0^t \mathrm{d}t_1\int_0^{t_1}\mathrm{d}t_2\;\big[\hat{\mathcal{H}}_{\mathrm{MS}}(t_1),\,\hat{\mathcal{H}}_{\mathrm{MS}}(t_2)\big] \tag{2.109}$$

and evaluating the time-ordered double integral using

$$\int_0^t \mathrm{d}t_1\int_0^{t_1}\mathrm{d}t_2\;\sin\big(\Delta_j(t_1-t_2)\big) = \frac{\Delta_j t-\sin(\Delta_j t)}{\Delta_j^2}, \tag{2.110}$$

we obtain

$$\hat{M}_2(t) = -i\sum_{i=1}^{N}\sum_{k=1}^{N}\Theta_{ik}(t)\,\hat{\sigma}_x^{(i)}\hat{\sigma}_x^{(k)}, \tag{2.111}$$

where the accumulated geometric phase is

$$\Theta_{ik}(t) = \sum_{j=1}^{N}\frac{\Omega_i\eta_{ij}\,\Omega_k\eta_{kj}}{4\Delta_j^2}\big(\Delta_j t-\sin(\Delta_j t)\big). \tag{2.112}$$

This term contains no motional operators; it is a purely geometric phase proportional to the area enclosed by the phase-space trajectory $\alpha_{ij}(t)$ up to time t.

Exact propagator. Collecting $\hat{M}_1$ (2.102) and $\hat{M}_2$ (2.111), the exact time-evolution operator is

$$\hat{U}_{\mathrm{MS}}(t) = \exp\left[\sum_{i=1}^{N}\sum_{j=1}^{N}\hat{\sigma}_x^{(i)}\Big(\alpha_{ij}(t)\,\hat{a}_j^\dagger - \alpha_{ij}^*(t)\,\hat{a}_j\Big) - i\sum_{i=1}^{N}\sum_{k=1}^{N}\Theta_{ik}(t)\,\hat{\sigma}_x^{(i)}\hat{\sigma}_x^{(k)}\right]. \tag{2.113}$$

The first term generates spin-dependent displacements of the motional modes, while the second describes the effective spin–spin interaction responsible for entanglement generation. Since $[\hat{M}_1, \hat{M}_2] = 0$ (the commutator of the first term containing bosonic operators with $\hat{M}_2$ of only spin operators vanishes because bosonic and spin operators act on separate Hilbert spaces, and all $\hat{\sigma}_x$ operators commute among themselves), the exponential factorises exactly,

$$\hat{U}_{\mathrm{MS}}(t) = \prod_{j=1}^{N}\hat{D}_j\Big(\sum_{i=1}^{N}\alpha_{ij}(t)\,\hat{\sigma}_x^{(i)}\Big)\ \exp\left[-i\sum_{i=1}^{N}\sum_{k=1}^{N}\Theta_{ik}(t)\,\hat{\sigma}_x^{(i)}\hat{\sigma}_x^{(k)}\right], \tag{2.114}$$

where $\hat{D}_j$ is the displacement operator from (2.46) for motional mode j.

2.3.3 Entanglement generation

Assuming constant parameters of Ω, η, and Δ, the propagator (2.114) reduces to

$$\hat{U}_{\mathrm{MS}}(t) = \hat{D}\big(\alpha(t)\hat{S}_x\big)\ \exp\big[-i\,\Theta(t)\,\hat{S}_x^2\big], \tag{2.115}$$

where $\hat{S}_x = \hat{\sigma}_x^{(1)} + \hat{\sigma}_x^{(2)}$ from (2.108) and

$$\alpha(t) = \frac{\Omega\eta}{2\Delta}\big(e^{-i\Delta t} - 1\big), \qquad \Theta(t) = \frac{(\Omega\eta)^2}{4\Delta^2}\big(\Delta t - \sin(\Delta t)\big). \tag{2.116}$$

We then consider two ions initialized in their electronic ground states, coupled to a single shared motional mode initially in the vacuum state,

$$|\psi(0)\rangle = |00\rangle \otimes |0\rangle_n\,. \tag{2.117}$$

It is convenient to decompose the spin state in the $\hat{\sigma}_x$ eigenbasis so that,

$$|00\rangle = \frac{1}{2}\Big(|{+}{+}\rangle_x - |{+}{-}\rangle_x - |{-}{+}\rangle_x + |{-}{-}\rangle_x\Big). \tag{2.118}$$

An eigenstate $|s_1 s_2\rangle_x$ satisfies $\hat{S}_x\,|s_1 s_2\rangle_x = (s_1 + s_2)\,|s_1 s_2\rangle_x$. The displacement operator $\hat{D}\big(\alpha(t)\hat{S}_x\big)$ couples the spin and motional degrees of freedom through its operator-valued

argument. However, when acting on a spin eigenstate, $\hat{S}_x$ can be replaced by its eigenvalue $(s_1 + s_2)$. Consequently, its action factorizes as

$$\hat{D}\big(\alpha(t)\hat{S}_x\big)\big(|s_1 s_2\rangle_x \otimes |0\rangle_n\big) = |s_1 s_2\rangle_x \otimes \big|(s_1 + s_2)\,\alpha(t)\big\rangle_n, \tag{2.119}$$

showing that the motional state undergoes a displacement with amplitude conditioned on the spin configuration as in Fig. 2.4b. Applying the displacement operator of $\hat{U}_{\mathrm{MS}}(t)$ to the initial state (2.118) yields

$$\begin{aligned}|\psi(t)\rangle = \frac{e^{-i\Theta(t)\hat{S}_x^2}}{2}\Big(&|{+}{+}\rangle_x\,|{+}2\alpha(t)\rangle_n - |{+}{-}\rangle_x\,|0\rangle_n \\ &- |{-}{+}\rangle_x\,|0\rangle_n + |{-}{-}\rangle_x\,|{-}2\alpha(t)\rangle_n\Big).\end{aligned} \tag{2.120}$$

At intermediate times $\alpha(t) \neq 0$, spin and motion are entangled, since each spin configuration is correlated with a distinct motional coherent state. The loop-closure condition

$$\alpha(T) = 0 \quad \Longrightarrow \quad T = \frac{2\pi}{\Delta} \tag{2.121}$$

disentangles the motion and leaves a purely spin operation,

$$\hat{U}_{\mathrm{MS}}(T) = e^{-i\,\Theta(T)\,\hat{S}_x^2}, \qquad \Theta(T) = 2\pi\left(\frac{\Omega\eta}{2\Delta}\right)^2. \tag{2.122}$$

Using $\hat{S}_x^2 = 2\hat{I} + 2\hat{\sigma}_x^{(1)}\hat{\sigma}_x^{(2)}$ and absorbing the global phase arising from the identity term,

$$\hat{U}_{\mathrm{MS}}(T) \sim \exp\big[-2i\,\Theta(T)\,\hat{\sigma}_x^{(1)}\hat{\sigma}_x^{(2)}\big]. \tag{2.123}$$

Acting on $|00\rangle_S$ gives

$$|\psi(T)\rangle = \cos\big(2\Theta(T)\big)\,|00\rangle - i\sin\big(2\Theta(T)\big)\,|11\rangle\,, \tag{2.124}$$

which is a superposition of $|00\rangle$ and $|11\rangle$ with the motional mode fully disentangled. The gate is maximally entangling when $2\Theta(T) = \pi/4$, requiring

$$\frac{\Omega\eta}{\Delta} = \frac{1}{2}. \tag{2.125}$$

Under this condition, the output state

$$\hat{U}_{\mathrm{MS}}(T)\,|00\rangle_S = \frac{1}{\sqrt{2}}\big(|00\rangle - i\,|11\rangle\big)_S \otimes |0\rangle_n \tag{2.126}$$

is a maximally entangled Bell state, with the motional mode fully disentangled from the electronic states. The population dynamics of this process are shown in Fig. 2.4c, where P_{00} and P_{11} reach equal populations of 0.5 at the gate time $t_{\text{gate}} = T$, where T is the time for a single full loop closure from (2.121).

The theoretical framework developed in this chapter establishes the quantitative link between the physical trap and the fidelity of quantum gate operations. The pseudopotential analysis shows that the trapping geometry directly sets the radial secular frequency ω_{rad}, which in turn governs both the Lamb–Dicke parameter η and the sideband Rabi frequencies Ω_{rsb} and Ω_{bsb} that drive the MS interaction. Any deviation of the trapping potential from a perfect harmonic well introduces a phonon-number-dependent shift in ω_r during the gate, causing the phase-space trajectory of Eq. (2.121) to fail to close exactly, leaving a residual spin-motion entanglement at the gate time [39]. Simultaneously, the laser must deliver a pulse of precisely defined frequency, phase, and duration to each ion site to realize the $\pi/2$-pulse and sideband transitions required by the MS protocol. These two requirement, a harmonic trapping potential and precise, individually addressed optical control, motivates the two engineering investigations that form the core of this thesis: the comparative analysis of scalable trap geometries in Chapter 3, and the development of a photonic integrated circuit for programmable laser delivery in Chapter 4.

Chapter 3
TRAP GEOMETRY

Traditionally, trapped-ion experiments use a macroscopic linear Paul trap shown in Fig. 2.2 in Section 2.1.2 with a deep and harmonic trapping potential [31]. However, the bulky structure limits the number of qubits in a given volume. 2D surface-electrode traps have emerged as an alternative to the traditional 3D Paul trap [40] and are currently the prevailing choice for trapped-ion experiments due to their versatility and scalability. Indeed, surface traps underpin the most advanced trapped-ion quantum information processors to date, enabling high-fidelity quantum computing demonstrations with tens of qubits [41, 42, 43, 44, 45, 13] including initial demonstrations towards fault-tolerant encoding [13] and operation [46]. Still, the field remains far from a utility-scale trapped-ion quantum processor.

Though many factors hinder the scalability of trapped-ion quantum technologies, here we focus on the effect of the trap electrode geometry on gate performance and power dissipation. We begin by introducing three candidate trap geometries and the simulation framework used to characterize them. We then investigate why the shaping of the trapping potential, and specifically its deviation from a perfect harmonic well, has a direct impact on entangling gate fidelity (Section 3.1). This motivates the set of figures of merit (FoM) developed in Section 3.2, which we subsequently use to compare the expected experimental performance (Section 3.3) and practicality (Section 3.4) of the three designs.

3.1 Trap Geometries and Simulation Methods

The geometry of the rf electrodes fixes the shape and confinement of the radial trapping potential, which in turn directly impacts the fidelity of laser-driven gate operations. As seen from Section 2.3, motional frequencies of ions have an intimate effect on entanglement. While there are entangling gate schemes that do not use the motional modes [47, 48], or

that can be run arbitrarily fast [49, 50], many platforms currently rely on gates with a speed limit set by the radial trap frequency [51]. Moreover, a higher trap frequency will reduce gate errors due to electric field noise [52]. However, the requirement to trap many ions in high-radial-frequency potentials suggests that power dissipation may become a problem if not accounted for during trap optimization. Any scalable trap geometry must therefore balance high trap frequency, low power dissipation, industrial reproducibility, and sufficient optical access for the necessary control beams.

Electrode Configurations With these constraints in mind, we consider three distinct trap geometries for their suitability for scaling trapped-ion quantum systems, shown in Fig. 3.1: a surface trap (Fig. 3.1a) [40], a "gnd-surface" trap consisting of the same surface trap with an added ground plane above the electrodes (Fig. 3.1b), and a miniature linear Paul trap, or "cross-rf" trap (Fig. 3.1c). We do not fully optimize the trap geometries, but rather explore the effect of wafer separation h on the trapping field for the two multi-wafer designs. We restrict our discussion to the scaling of the radial trapping potential, as this is completely defined during trap fabrication, while the axial trapping field is set post-fabrication by the voltages applied to the dc electrodes. We will generally apply an rf-source of amplitude $V_{\mathrm{rf}} = 10$ V and drive frequency $\Omega_{\mathrm{rf}} = 2\pi \times 20$ MHz.

Simulation Method We simulate the electric field due to each rf electrode to obtain the pseudopotential for a given geometry using COMSOL Multiphysics with the boundary element (BE) method. In the BE method, the boundary constraints defined by the electrodes are used to define the integral form of Maxwell's equations for the structure of interest, which are then solved on a pre-defined mesh. This method has been validated against experiments in several previous studies [53, 54, 55, 56, 57, 58]. The full simulation volume is $8 \times 8 \times 5\,\mathrm{mm}^3$, meshed with a built-in adaptive routine at an element size of 100 µm. A finer meshing volume of $0.6 \times 0.6 \times 0.5\,\mathrm{mm}^3$ is centered at the expected rf-null point, with element sizes of 1–10 µm and a minimum of 1 µm at the ion location. This ensures that meshing errors remain smaller than errors due to fabrication imperfections. Each simulation takes approximately half an hour to run. In the following sections, the trapping performance of each trap geometry is

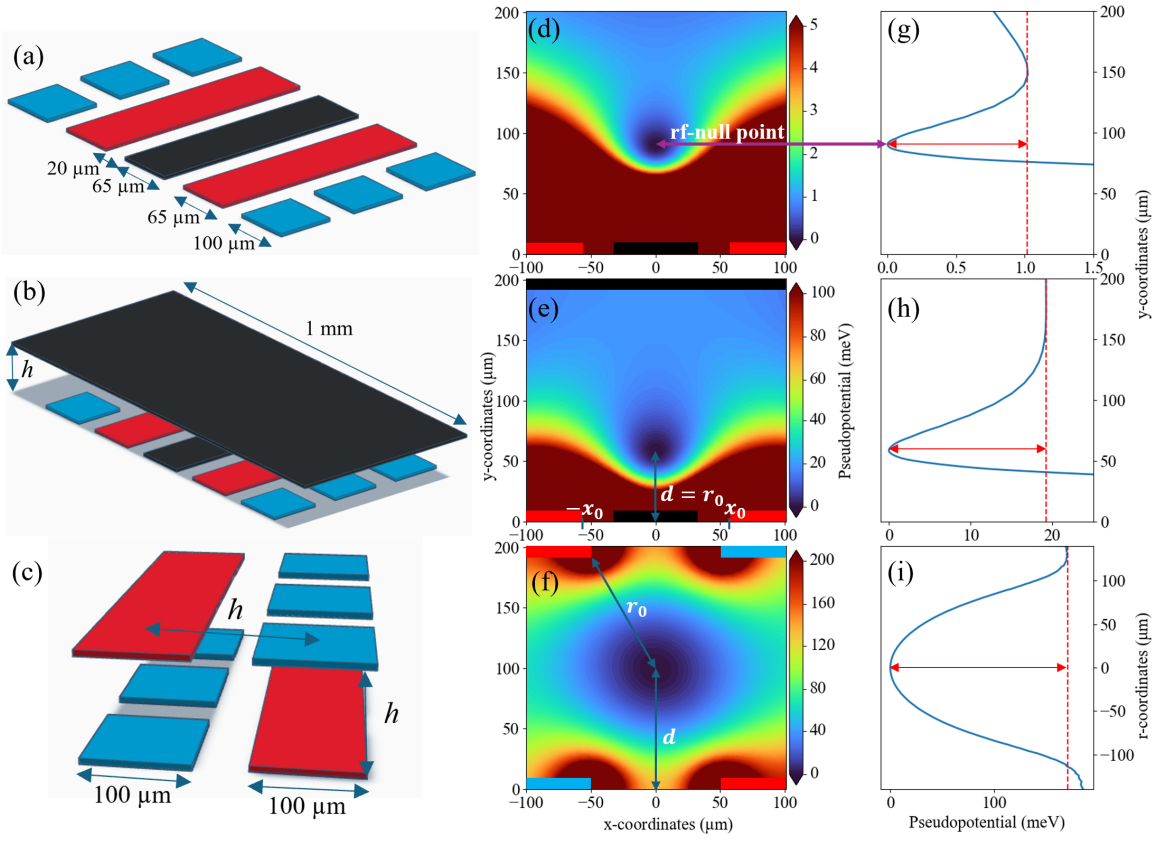

Figure 3.1: (a-c) Electrode geometries for the surface trap, "gnd-surface" trap, and "cross-rf" trap, respectively. rf electrodes are shown in red, dc electrodes in blue, and grounded electrodes in black. The parameter h denotes the wafer separation in the two multi-wafer designs and is varied. (d-f) Two-dimensional pseudopotential maps of the x-y radial cross-section at $z = 0$ for the geometries in (a-c), respectively. The rf-null point marks the ion equilibrium position above the electrode plane define as $y = d$. The distance from the ion to the nearest electrode-surface is r_0 and x_0 is the distance from nearest rf rail to the origin. (g-i) One-dimensional pseudopotential slices at $z = 0$, $x = 0$ for (a-b), and along $r = \sqrt{x^2 + y^2}$ for (c), used to extract the trap depth. The red dashed line marks the saddle point of the pseudopotential, whose value relative to the rf-null minimum defines the trap depth and sets the maximum ion kinetic energy before escape.

investigated for varying wafer separation h; for the cross-rf trap, the horizontal electrode-electrode spacing is also kept at h to maintain the symmetry of the potential (see Fig. 3.1c), while all other parameters are kept constant.

The Effects of Trapping Potential on Optical Gates

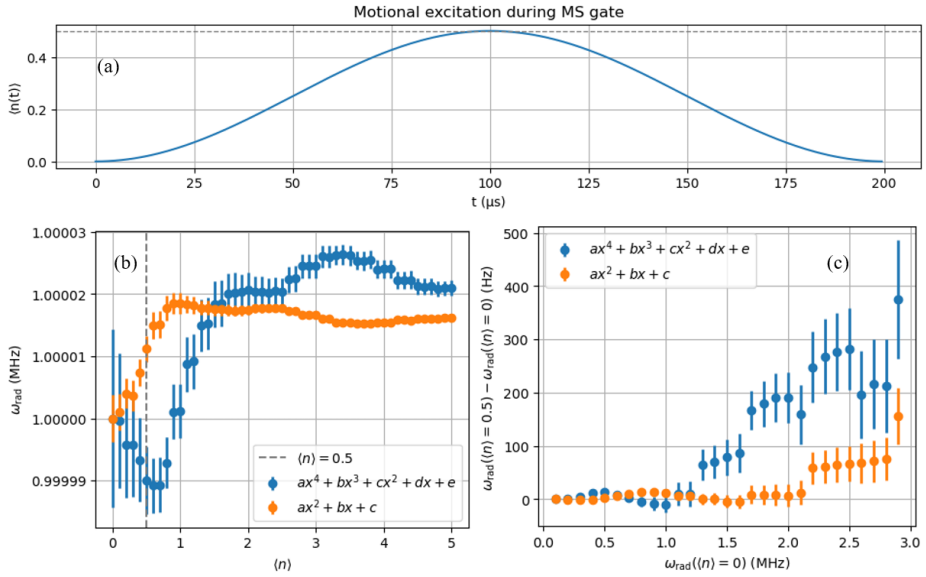

Figure 3.2: (a) Mean phonon number $\langle n\rangle$ as a function of time during the MS gate, tracing the phase-space loop of Fig. 2.4(b). The motional excitation increases and returns to zero at t_{gate}, with a maximum occupation of $\langle n\rangle = 0.5$. (b) Radial trap frequency ω_{rad} as a function of mean phonon number $\langle n\rangle$, fitted with quadratic $(ax^2 + bx + c)$ and quartic $(ax^4+bx^3+cx^2+dx+e)$ polynomials. (c) Anharmonicity-induced frequency shift $\omega_{\text{rad}}(\langle n\rangle = 0.5) - \omega_{\text{rad}}(\langle n\rangle = 0)$ as a function of the ground-state trap frequency $\omega_{\text{rad}}(\langle n\rangle = 0)$. The quartic fit, which is a better approximation of a real trapping potential and shows significant frequency shifts, motivates the harmonicity figure of merit introduced in Section 3.2.2.

Before defining the FoM used to compare the three trap geometries, we first establish the link between the trapping potential and the laser-based operation, specifically entanglement. During the MS gate with the time propagator (2.114), the spin-dependent displacement

drives the ions into excited motional states. The excitation reaches its maximum at $t_{\text{gate}}/2$, corresponding to the largest phase-space displacement, and returns to the initial state at t_{gate} when the trajectory closes. This behaviour is shown in Fig. 3.2a, where the mean phonon number $\langle n(t)\rangle$ peaks at $\langle n\rangle = 0.5$, consistent with the displacement amplitude $|\alpha_{\text{MS}}(T/2)|$ given the MS gate condition in Eq. (2.125). Each phonon number corresponds to a characteristic spatial spread of the motional wavefunction, as given by Eq. (2.45).

To quantify how trap anharmonicity affects laser-driven gate operations, we consider two key aspects: (i) how the effective curvature of the trapping potential, used to extract the radial trap frequency via Eq. (2.21), changes as the ion moves through different Fock states during the MS gate, and (ii) how this curvature differs when extracted using harmonic (quadratic) versus anharmonic (quartic) approximations to the potential. We simulate a surface-electrode trap with COMSOL Multiphysics similar to the one in Fig. 3.1a, but with a spatial resolution of 0.1 nm. For a ground-state radial trap frequency of $2\pi \times 1$ MHz, the corresponding wavefunction spread is $\sigma_0 \approx 11.2$ nm. We perform the analysis along the y-direction, which exhibits the weakest symmetry and is therefore most sensitive to anharmonic effects.

Figure 3.2b shows the extracted radial trap frequency as a function of phonon occupation number. As $\langle n\rangle$ increases, the spatial extent of the wavefunction grows, and this spread defines the region over which the potential is fitted to extract its curvature. For both quadratic (blue) and quartic (orange) fits, the variation in trap frequency over the range $\langle n\rangle = 0$ to 5 remains on the order of tens of Hz, which is negligible compared to the MHz-scale trapping frequency. At $\langle n\rangle = 0.5$, the error bars for different fitting models do not overlap indicating a statistically significant shift that depends on both the motional state and the anharmonicity of the trapping potential.

A more pronounced effect emerges when comparing the frequency shift between the maximally excited state ($\langle n\rangle = 0.5$) and the ground state across different baseline trap frequencies, as shown in Fig. 3.2c. The frequency shift increases with the ground-state trap frequency and can reach several hundred Hz, particularly when using the quartic fit, which more accurately captures the anharmonicity of the trapping potential. While higher ground-state trap frequencies are generally desirable [59], this reveals an important trade-off:

increasing the trap frequency also amplifies the sensitivity of the system to anharmonicity during the MS gate. Frequency shifts on the order of hundreds of Hz are sufficient to introduce detuning errors in the MS interaction that can limit gate fidelities below the fault-tolerant threshold of 99.99%.

This analysis provides strong motivation for minimizing trap anharmonicity, which we now formalize, together with ion height, trap depth, and trap frequency, as the FoM used to compare the scalability of the three geometries.

3.2 Figures of merits

We evaluate the three designs through three figures of merit (FMs): harmonicity k^{rf} (Section 3.2.2), trap depth D (Section 3.2.3), and radial trapping frequency ω_{rad} (Section 3.2.4). Before introducing these, we first discuss the ion height, which, while not a direct figure of merit, influences several of the quantities defined below.

3.2.1 Ion Heights

The ion height, d, is the vertical distance between the rf-null point and the bottom wafer, as indicated in Figs. 3.1d-f. The position of the rf null does not directly impact the scalability of a trapped-ion system, but it does influence the achievable trap frequency (Section 3.2.4) and heating rate (Section 3.3) and has implications for optical addressing [60, 61]. We note that d can also be controlled by changing the lateral geometry of the electrodes [62], but here we focus on the relationship between trapping height d and wafer separation h for the multi-wafer traps.

Fig. 3.3 presents the ion height d derived from simulations as a function of h, the distance between wafers. The trap height for the surface trap is shown in red for reference. Our uncertainty for the estimation of d is defined by our mesh size of 1 µm. This uncertainty could be reduced with interpolation or a finer mesh. For the cross-rf trap, the rf-null point is always directly between the two wafers, or $d = h/2$. As expected, as h increases, the rf-null point of the gnd-surface trap approaches that of the bare surface trap.

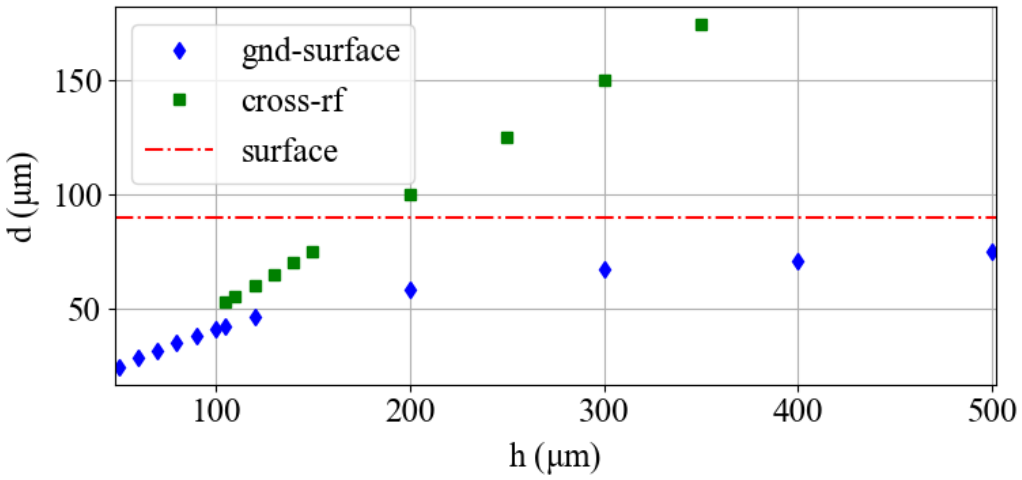

Figure 3.3: Ion height d as a function of wafer separation h for the gnd-surface and cross-rf trap geometries, with the surface trap shown as a reference. Both multi-wafer designs show an increasing d with h, as the growing electrode separation pushes the rf-null point further from the substrate.

3.2.2 Harmonicity

Harmonicity, k, measures how closely the trapping field resembles an ideal harmonic potential. From Eq. (2.9) in Section 2.1.2, $k_x^{rf} = -k_y^{rf} = 1$ for a perfect quadrupole field. Deviations from this can cause gate errors due to increased cross-Kerr nonlinearity [63, 64], and the entangling gate control must be optimized with the particular anharmonicity in mind [65]. Anharmonicity also reduces the achievable trap frequency for a given drive voltage in two ways. First, it reduces the amount of applied voltage converted to a quadratic trapping potential as described in (2.21). It also reduces the experimentally accessible extent of the stability region of the dynamic trapping field [66, 67, 68]. A full multipole expansion of the field can provide further insight into the expected ion dynamics and provide corrections to the trap frequencies [69], but here we only consider harmonicity.

We determine radial harmonicity by performing a quadratic fit of the electric potential along the two radial axes. For the multi-wafer traps, we investigate how harmonicity changes with wafer separation h. The cross-rf trap is symmetric and we conducted the fit along the

diagonal axis as describe in Fig. 3.1i. For the surface and gnd-surface traps, $k_y < k_x$ due to the asymmetry of the y-axis. Fig. 3.4 shows $k_y^{\mathrm{rf}} = k$ as a function of h for the two multi-wafer traps. The error bars derived from the quadratic fit are smaller than the symbol size and are all less than 0.001.

The surface trap design (red line) suffers from large anharmonicity due to the highly non-symmetric geometry. The gnd-surface trap exhibits a modest increase in harmonicity in comparison to the surface trap for most heights. However, it suffers a steep decrease in k when h is less than the rf-rf electrode distance. For large separation, the configuration effectively transitions into a surface-electrode trap. In contrast, the harmonicity of the cross-rf trap is inversely proportional to h and is generally high due to its symmetric geometry.

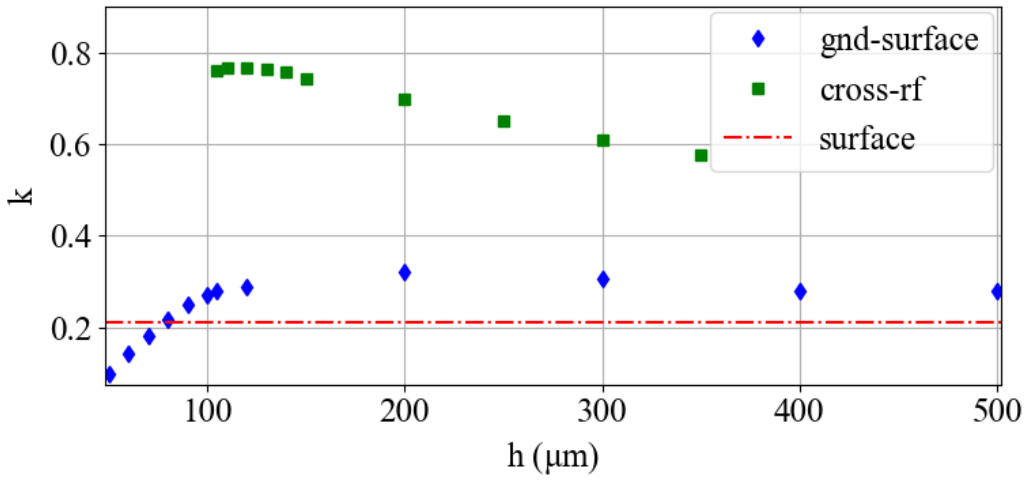

Figure 3.4: Harmonicity k, defined from the 2nd-order coefficient of a quadratic fit to a radial electric potential (with $k = 1$ for a perfect quadrupole), as a function of wafer separation h for the gnd-surface and cross-rf traps, with the surface trap shown for reference. A larger k indicates a more harmonic potential, in which the cross-rf trap substantially outperforms both designs, owing to its symmetric electrode geometry, though k decreases with h. The gnd-surface trap improves modestly over the surface trap reference for h greater than the rf–rf electrode spacing, but drops sharply below it at smaller h where wafer proximity breaks the near-quadrupole symmetry.

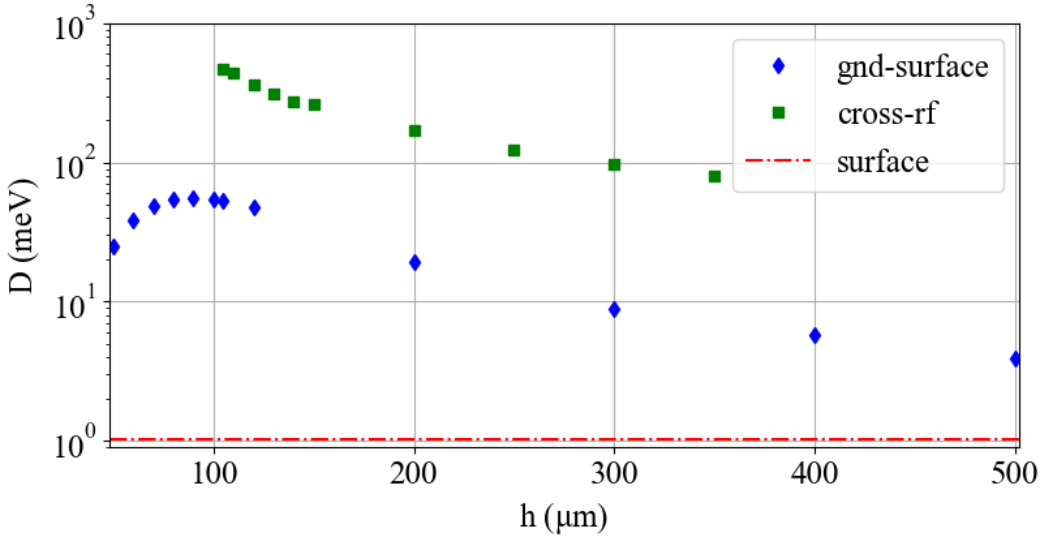

Figure 3.5: Trap depth D as a function of wafer separation h for the gnd-surface and cross-rf trap designs, with the surface trap shown as a reference ($D \approx 1$ meV). The logarithmic scale spans nearly three orders of magnitude, highlighting the improvement of both multi-wafer designs over the conventional surface trap.

3.2.3 Trap depth

The trap depth D is the minimum potential energy difference between the rf-null point and the saddle point, which is indicated by a red arrow in Figs. 3.1g-i. D defines the maximum kinetic energy an ion can have without escaping confinement. Low trap depth can hinder ion loading and increase ion loss due to background gas collisions [70, 55]. As above, we only consider the contribution from the rf trapping fields and do not consider the effect of the dc potential, as that is determined post-fabrication by the voltages applied to the dc electrodes.

Fig. 3.5a shows the relationship between D and h for the multi-wafer traps. The trap depth for the surface trap design is shown in red. We use the same trapping parameters as in previous sections, $\Omega_{\mathrm{rf}} = 2\pi \times 20\,\mathrm{MHz}$ and $V_{\mathrm{rf}} = 10\,\mathrm{V}$. For both multi-wafer traps D generally increases with decreasing h. Though again the field of the gnd-surface trap is distorted when the wafer height is less than the rf-rf electrode separation, reducing D.

3.2.4 Trap frequency

In an ideal harmonic system, the first stability region of the Matthieu equation spans the entire range $0 \leq q \leq 1$ [32, 67] and ideally Ω_{rf} and V_{rf} would be chosen such that $q \simeq 1$ increases the trap frequency achievable for a given voltage, as illustrated in Fig. 3.6b. However, for surface traps, the trap frequency is generally kept at $\omega < 0.1\Omega_{\text{rf}}$, or $q < 0.3$ [71, 31] to achieve stable trapping. This deviation from the ideal case is attributed to the anharmonicity of the trap, which is not captured by the idealized potential derived from the Matthieu Equation [35]. Thus, the achievable radial trap frequency depends on the trap geometry through both the harmonicity k and the trapping position r_0.

The cross-rf wafer trap is symmetric along the principle radial axes indicated in Fig. 3.1i. For the surface and the gnd-surface wafer trap we simply focus on the radial frequency ω_y to be consistent with the axis we have chosen for harmonicity and trap depth. Fig. 3.6a shows the radial frequency of a $^{40}Ca^{+}$ ion in the three trap designs for $\Omega_{\text{rf}} = 2\pi \times 20\,\text{MHz}$ and $V_{\text{rf}} = 10\,\text{V}$. As above, we vary the wafer separation h for the two multi-wafer trap designs. The trap frequency for the surface trap under the same drive parameters is shown in red as a reference.

The trap frequency generally increases with smaller h, although trap frequency reduces when h is less than the electrode-electrode separation for the gnd-surface trap. Fig. 3.6(b) shows the relationship between Ω_{rf}, the q-parameter, and the trapping frequency for the three trap designs for $V_{\text{rf}} = 10\,\text{V}$. For the two multi-wafer traps $h = 105\,\mu\text{m}$ as marked in Fig. 3.6(a). At the same q, the multi-wafer traps produce a higher radial trap frequency, with the cross-rf trap having a slightly better performance. High trap depth [67] and high harmonicity [72] allow for certain traps to operate at much higher instability q value, increasing the attainable radial trap frequency [72].

Trap frequency can be increased by increasing the trap drive amplitude,V_{rf}. However, the maximum voltage is set by the breakdown field of the dielectric used to separate neighboring electrodes [73]. Moreover, for large-scale trapped-ion systems, increased rf amplitude and frequency will increase power dissipation, which can be limiting, especially for systems working at cryogenic temperatures. This is discussed further in Section 3.3. Therefore, it

is important to understand the maximum trap frequency that can be achieved given a set drive amplitude.

Fig. 3.6c shows the maximum achievable frequency for $V_{\mathrm{rf}} = 10\,\mathrm{V}$ as a function of h. To find this, we pick an operating q parameter for each trap by scaling a typical working parameter for surface traps ($q = 0.250$) with the harmonicity of each design, e.g. $q = q_{\mathrm{st}} \frac{k}{k_{\mathrm{st}}}$ [32]. This results in $q = 0.905$ for the cross-rf trap, matching recent results in a miniature 3D-printed trap [72], and a more modest $q = 0.333$ for the gnd-surface trap. These q parameters are indicated in Fig. 3.6b. This q parameter then defines the drive frequency for a given V_{rf} with (2.16). These parameters then give the maximum achievable trap frequency for a given rf drive amplitude from (2.21). As seen in Fig. 3.6c, the multi-wafer traps show a gain in maximum trap frequency due to the increased harmonicity. In particular, the cross-rf trap provides a more than 10x improvement over the surface trap design considered here (6.12 MHz vs 1.00 MHz). For the gnd-surface trap in particular, we find that the maximum trap frequency (2.84 MHz) is achieved when the wafer height equals the rf-rf electrode separation. These results can be used to focus design optimization for other electrode geometries and highlight the importance of the harmonicity of the trapping potential.

3.3 Expected Experimental Performance

In this section we explore the expected experimental performance of the three trap designs. We use the field-dependent parameters presented above to understand the expected heating rate and how the necessary voltage and expected power dissipation scales with target trap frequency.

3.3.1 Heating Rate

Noisy electric fields at frequencies near the secular trap frequency ω_r cause a time-dependent increase in the thermal population of an ion's motional modes [74, 75], causing entangling gate errors [76]. The origin of electric field noise is not well understood [52], but the average

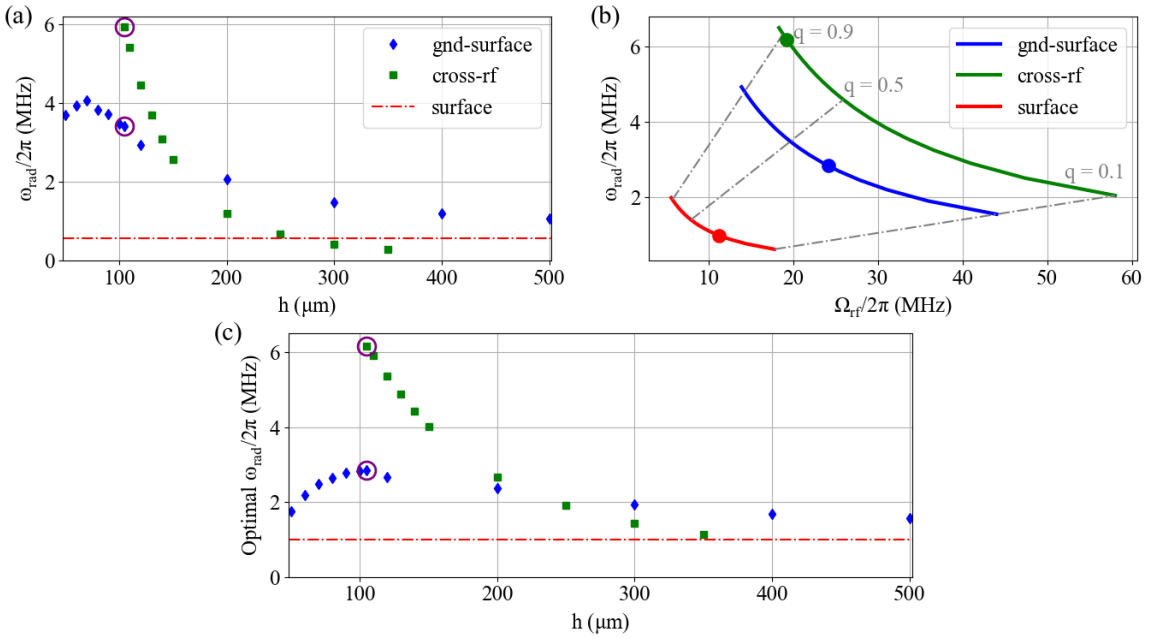

Figure 3.6: (a) Radial trap frequency ω_{rad} as a function of wafer separation h for the multi-wafer trap designs with the surface trap shown for reference. Both multi-wafer designs substantially exceed the surface trap, with frequencies generally increasing at smaller h as the electrode geometry improves harmonicity and reduces r_0. The gnd-surface trap drops sharply when h falls below the rf–rf electrode spacing, consistent with the harmonicity degradation seen in Fig. 3.4. (b) Radial trap frequency as a function of Ω_{rf} at $V_{\mathrm{rf}} = 10\,\mathrm{V}$ for the three trap geometries at fixed $h = 105\,\mu\mathrm{m}$ for the multi-wafer designs. Gray dashed lines indicate constant instability parameter q; the filled points mark the harmonicity-scaled operating q used in (c) ($q = 0.905$ for cross-rf, $q = 0.333$ for gnd-surface, $q = 0.250$ for surface). At equal q, the multi-wafer traps achieve higher ω_{rad}, demonstrating that improved harmonicity directly enables higher trap frequencies for a given drive. (c) Maximum achievable radial frequency at $V_{\mathrm{rf}} = 10\,\mathrm{V}$ as a function of h, using the harmonicity-scaled q from (b). The cross-rf trap achieves a more than 10× improvement over the surface trap (6.12 MHz vs. 1.00 MHz) at $h = 105\,\mu\mathrm{m}$, while the gnd-surface trap peaks at 2.84 MHz when h equals the RF–RF electrode separation. Purple circles in (a) and (c) mark the $h = 105\,\mu\mathrm{m}$ operating point used in Section 3.3.

increase in phonon number, or the heating rate $\dot{\bar{n}}$, generally fits the following trend [52]:

$$\dot{\bar{n}} \propto \omega_r^{-2} r_0^{-4} \tag{3.1}$$

Unfortunately, ω and r_0 generally counteract each other as in Eq. (2.21). The expected heating rates of the three trap designs, normalized to the expected heating rate of a surface trap (Eq. (3.1)), are shown in Fig. 3.7. This indicates that with all other factors kept equal, the cross-rf trap would enjoy nearly an order of magnitude lower heating rate than the other two designs, and the gnd-surface trap can still achieve approximately half the heating rate of a surface trap. This may be negated by the introduction of more surface area, depending on the origin of the noise. Still, multi-wafer traps can help reduce the heating rate under the assumption that the electric field noise is not affected by trap geometry.

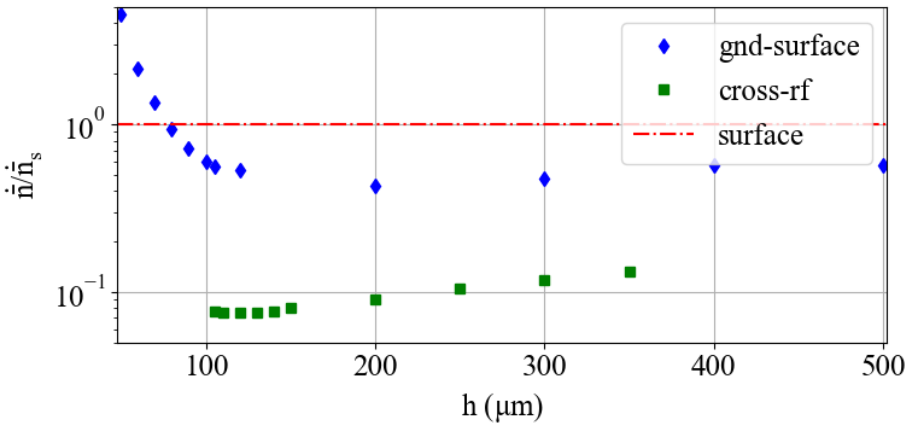

Figure 3.7: Motional heating rate $\dot{\bar{n}}$ for the multi-wafer trap designs, normalized to the surface trap heating rate $\dot{\bar{n}}_s$, as a function of wafer separation h. The heating rate is estimated from the empirical scaling $\dot{\bar{n}} \propto \omega_r^{-2} r_0^{-4}$, where the competing dependences on trap frequency and electrode distance are set by each geometry. The cross-rf trap achieves nearly an order of magnitude reduction in heating rate across most of the range studied, while the gnd-surface trap's improvement depends heavily on h.

3.3.2 Achieving a Target Trap Frequency

Here we compare the performance of the surface trap design and the two multi-wafer traps when $h = 105\,\mu\text{m}$ (highlighted in Fig. 3.6). This wafer height provides both high harmonicity and large trap frequency for both multi-wafer trap designs. The rf-null position d and harmonicity k are set by the trap geometry. We use the operating q parameters found in Section 3.2.4 and reported in Table 3.1. Here, we use the values of d, k, and q to calculate the minimum trap voltage and drive frequency needed to achieve a target trap frequency of $\omega_{\text{rad}} = 2\pi \times 10\,\text{MHz}$ using Eq. (2.21) and Eq (2.16). This is summarized in Table 3.1. This example underlines the importance of harmonicity again – as in Fig. 3.6(c), a higher harmonicity reduces the necessary source voltage and frequency by increasing the workable q parameter and by improving the conversion efficiency between applied voltage and trap frequency. Thus, the multi-wafer traps require significantly reduced drive voltage and frequency with respect to the surface trap geometry. This will be particularly important if trapped-ion systems are to increase the number of ions per chip.

The drive parameters define the expected power dissipation for each of the trap geometries. Power dissipation can occur due to electrical and dielectric losses. Here we focus on electrical power consumption as dielectric loss varies with material. COMSOL simulations show that the capacitance of the rf electrodes in the three trap designs are all around 0.1 pF ($C_{\text{surface}} = 91.0\,\text{fF}$, $C_{\text{gnd-surface}} = 115.0\,\text{fF}$, and $C_{\text{cross-rf}} = 89.5\,\text{fF}$). In practice, the capacitance will likely be dominated by the trace layout and external wiring with standard values on the order of 10 pF [77, 78, 79, 61]. Thus we present the power dissipation normalized to the system capacitance, which scales with the amplitude and frequency of the rf drive [80]:

$$P \propto V_{\text{rf}}^2 \Omega_{\text{rf}}^2. \tag{3.2}$$

As seen in Table 3.1, the cross-rf (gnd-surface) trap will need orders-of-magnitude less power with respect to a surface trap due to reduced drive amplitude and frequency. This further highlights the need for high harmonicity to enable operation at $q \sim 1$.

Table 3.1: **Simulated experimental performance.** Experimental values of the investigated FoM and the heating and power scaling for each trap geometry. The errors on the reported values are discussed in the text and are limited by the resolution of the simulations which limits the estimation of d.

Geometry	d [µm]	k	q	$\omega_{\mathrm{rad}}/2\pi$ [MHz]	V_{rf} [kV]	$\Omega_{\mathrm{rf}}/2\pi$ [MHz]	$\bar{P}$ (norm)
surface	90	0.210	0.250	10	15	110	1
gnd-surface	46	0.280	0.333	10	4.0	85	4.0×10^{-2}
cross-rf	60	0.697	0.905	10	0.42	31	6.1×10^{-5}

3.4 Practicality

3.4.1 Fabrication

Sections 3.1 and 3.3 suggest that the two multi-wafer designs present a path forward to achieving significantly reduced power dissipation for a given target trap frequency, a key to increasing the number of trap sites in a trapped-ion quantum computer. However, multi-wafer traps complicate fabrication and reduce the overall optical access. Here, we consider how the increased complexity of the multi-wafer traps will affect the overall reliability and performance.

Surface-electrode ion traps can be fabricated using traditional clean-room microfabrication techniques [40]. Simple planar geometries are straightforward to make on a variety of different substrates, and advanced fabrication techniques have been leveraged to create complex surface electrode traps offering specific functionalities such as high optical access through the trap [61] and junctions between trapping zones [81, 82, 57, 83].

Multi-wafer traps are more difficult to fabricate that surface traps, but traps with geometries similar to the cross-rf trap discussed here have been demonstrated with a variety of different techniques. Solutions include manual wafer stacking [84, 85] and cleanroom-based MEMS techniques for monolithic ion traps [86]. Wafer alignment can be quite precise, with reported angular, lateral, and wafer separation errors of less than 0.05°, 2 µm, and 5 µm,

respectively for a 2 cm $\times$ 2 cm chip [85].

The gnd-surface trap is significantly simpler than the cross-rf multi-wafer trap and can take advantage of all the microfabrication techniques developed for high performance surface traps. The ground plane is unpatterned and thus lateral misalignment has no impact on the trap parameters. Errors in the trap height will change the ion position but will not distort the potential. Thus, though it provides more modest gains with respect to a surface trap the simplicity may improve repeatability and reliability

3.4.2 Optical Access

The main focus of this manuscript has been the effect of trap geometry on the radial trapping potential. However, a truly scalable architecture must also include optical control including fast control of the spectral, temporal, and spatial degrees of freedom across the visible spectrum [87]. In general, current experiments take advantage of the large optical access of well-engineered surface traps to excite ions with lasers parallel to the trap and collect fluorescence from the top hemisphere, which has unimpeded optical access. However, as architectures begin to tile trapping regions in a 2D plane [88, 44] this will not be sufficient. Instead, the optical control beams will likely need to come from below or above the trap. In surface traps, this has been achieved by integrating slits under the ions [61] or with integrated photonics and grating couplers [60, 89, 90, 91].

In previous demonstrations of multi-wafer traps similar to our cross-rf design, optical access was achieved through the opening between the rf and ground electrodes, both perpendicular and parallel to the wafers [85, 84, 86, 92, 93, 94]. In this case, the electrode-electrode separation will define the achievable numerical aperture for both excitation and fluorescence collection. The gnd-surface trap design does not naturally provide the same separation between electrodes for optical access. However, we propose two possible solutions. First, the ground plane could be made from a transparent wafer (e.g. borosilicate) with a grounded coating of a transparent conductive material such as indium-tin-oxide. This would enable all of the benefits laid out in the previous sections without a large change the optical access with respect to the surface trap. However, there will likely still be small reflections from

each interface, and care will have to be taken to reduce the effect of this stray light. Second, openings in the ground plane could be engineered for collection and excitation, similar to previous high optical access surface traps [61]. While this would change the electrical trap properties, co-optimization of electronic and optical properties is an opportunity for future work.

Meanwhile, rather than integrating photonic components directly into the trap substrate, an independent photonic integrated circuit (PIC) can provide flexible, programmable control of the gate beams while remaining compatible with any of the trap geometries discussed above. In the following chapter, we present such an approach: an FPGA-controlled silicon nitride PIC operating at 729 nm that targets the $4s\,^2S_{1/2} \leftrightarrow 3d\,^2D_{5/2}$ qubit transition of $^{40}Ca^+$ and is designed to scale to large numbers of independently addressed ions.

Chapter 4

LIGHT DELIVERY

The ability to precisely deliver and modulate laser light to individual ions in a trap is as central a challenge to scaling trapped-ion quantum computers as the trap geometry itself. As discussed in Chapter 2, laser-based gate operations require optical control across multiple ions, each of which must be individually addressed with high spatial and temporal resolution, along with spectral stability.

Two broad approaches to light delivery have emerged. Conventional free-space optical setups route laser beams through bulk optical elements such as acousto-optic modulators (AOMs), beam splitters, and mirrors [95, 21, 17]. AOMs offer fast, high-extinction modulation, but each additional ion channel requires its own dedicated optics and alignment procedure, and the resulting setups become increasingly difficult to stabilize, reproduce, and miniaturize as the number of ions grows. Trap-integrated photonic circuits offer a complementary set of advantages: many optical channels can be defined lithographically on the trap chip itself, dramatically improving scalability and alignment [60, 90, 89, 96, 97]. However, embedding photonics into the trap substrate couples the optical and electrical design constraints, complicating fabrication and limiting the flexibility to pair a given light delivery system with different trap geometries, a limitation that is especially relevant given the diversity of trap architectures explored in Chapter 3.

In this chapter, we present an alternative approach that combines the modularity of free-space optics with the scalability of integrated photonics: a standalone silicon nitride photonic integrated circuit (PIC), decoupled from the ion trap, operating at the 729 nm qubit transition of $^{40}Ca^{+}$ and controlled by a field-programmable gate array (FPGA). Because the PIC is an independent module connected to the trap only through free space or fiber optics, the same platform can be paired with any of the trap geometries discussed in Chapter 3 without redesigning the light delivery system.

4.1 Photonic Integrated Circuit

The PIC used in this work is a silicon nitride (Si_3N_4) atom-control photonic integrated circuit following the design of Menssen et al. [2]. Silicon nitride is chosen for its low optical loss, transparency across visible wavelengths—including the 729 nm qubit transition of $^{40}Ca^+$—and compatibility with CMOS fabrication processes. Figure 4.1a shows a wafer containing three PICs fabricated in parallel, illustrating the mass-producibility of the platform; the specific device used for characterization and future trapped-ion experiments is highlighted by the light blue box.

The core optical element is the dual-ring-assisted Mach–Zehnder modulator (DRMZM), shown in Fig. 4.1b. Each DRMZM consists of a Mach-Zehnder interferometer with a ring resonator coupled to each arm. In the overcoupled regime, each ring acts as a phase amplifier: the small phase shifts produced by fast but weak piezoelectric actuators are amplified to a full $\sim 2\pi$ phase shift per ring. By independently tuning the operating point of both rings, the amplitude and phase in each arm can be set to achieve destructive interference at the output, yielding extinction ratios exceeding 30 dB. This architecture is robust to fabrication variations, since the two tunable rings provide sufficient degrees of freedom to compensate for imperfections in the beamsplitter ratios that would otherwise limit extinction in a conventional Mach-Zehnder modulator [2].

Light is coupled into the chip through a 4×4 array of input grating couplers and exits through a 1×16 array of output grating couplers (Fig. 4.1c), with the input and output gratings oriented at 90° to enable separation via a polarizing beamsplitter. In the trapped-ion configuration, the output array maps directly onto a linear ion chain, with each channel addressing an individual ion site.

Slow (thermal) tuning. A resistive heater coil integrated alongside each ring resonator shifts the resonant wavelength via the thermo-optic effect. As fabricated, ring resonances are scattered over hundreds of picometers across the 16-channel array, making simultaneous operation at a single laser frequency impossible without correction. Thermal tuning provides the necessary picometer-scale adjustment to align all channels to a common operating

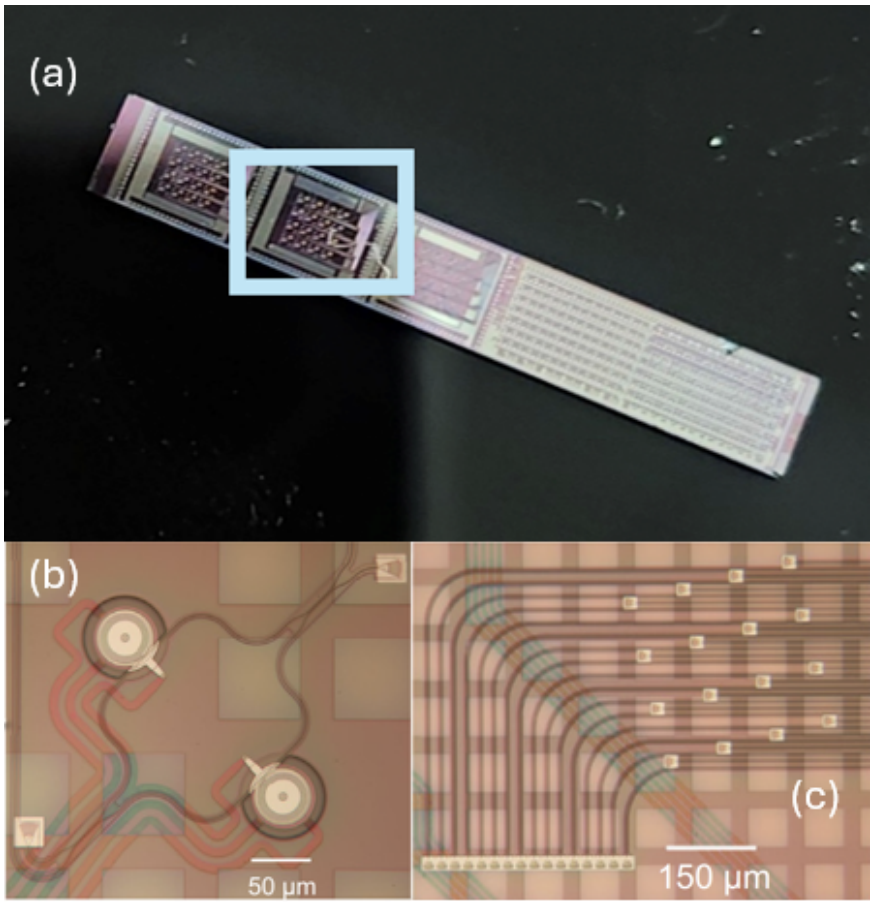

Figure 4.1: (a) Photograph of a silicon nitride (Si_3N_4) wafer containing three PICs fabricated in parallel; the device used in this work is highlighted with a blue box. (b) Microscope image of a single dual-ring-assisted Mach-Zehnder modulator (DRMZM), the core optical switching element of the PIC. (c) Microscope image of the input grating coupler array (4×4) and output grating coupler array (1×16), oriented at 90° to each other for polarization-based separation [2]. The 16-channel output array maps directly onto a linear ion chain, with each channel addressing an individual ion site.

wavelength. Once calibrated, the heater setpoints need only be updated to compensate for slow environmental drifts.

Fast (piezo-electric) modulation. Each ring is equipped with an aluminum nitride (AlN) piezoelectric actuator that mechanically deforms the waveguide, shifting the resonance on nanosecond timescales. Menssen et al. demonstrated voltage switching times of (5.8 ± 0.4) ns and pulse-area repeatability with a standard deviation of 9.8×10^{-4} over 1000 consecutive pulses at 780 nm, making the switching compatible with the single-qubit rotations and sideband transitions required for the Mølmer–Sørensen gate (Chapter 2). During gate operations, the thermal setpoint holds each resonator near the target wavelength while the fast piezoelectric channel rapidly toggles the transmission to define the pulse sequence.

4.2 Optical Setup and Characterization

Stable operation of the PIC requires that the input laser frequency be held constant relative to the qubit transition. The 729 nm laser is frequency-stabilized via a Pound–Drever–Hall (PDH) lock implemented with a Toptica laser system and a high-finesse reference cavity, keeping the laser linewidth well below the natural linewidth of the qubit transition (Section 2.1.1) and ensuring that frequency noise does not limit gate fidelity. The stabilized laser is locked to 729.129 nm, chosen to lie within the tunable range of the PIC resonators under thermal control.

The optical setup is shown in Fig. 4.2a–b and is built on a standard optical breadboard. The input beam passes through a half-wave plate (HWP) and a quarter-wave plate (QWP) to maximize coupling into the PIC. It then passes through a polarizing beamsplitter (PBS), which pickoffs a fraction of the beam for power monitoring, followed by two steering mirrors for alignment adjustment. A 2× objective focuses the beam onto the chip surface. Fine alignment between the beam and the on-chip grating input is achieved using a three-axis translation stage (Fig. 4.2c). Transmitted and reflected optical signals are monitored simultaneously by a photodiode, which provides real-time power measurements, and a camera, which images the near-field mode profiles at the chip outputs.

To align the PIC resonators with the stabilized laser, the chip temperature is regulated

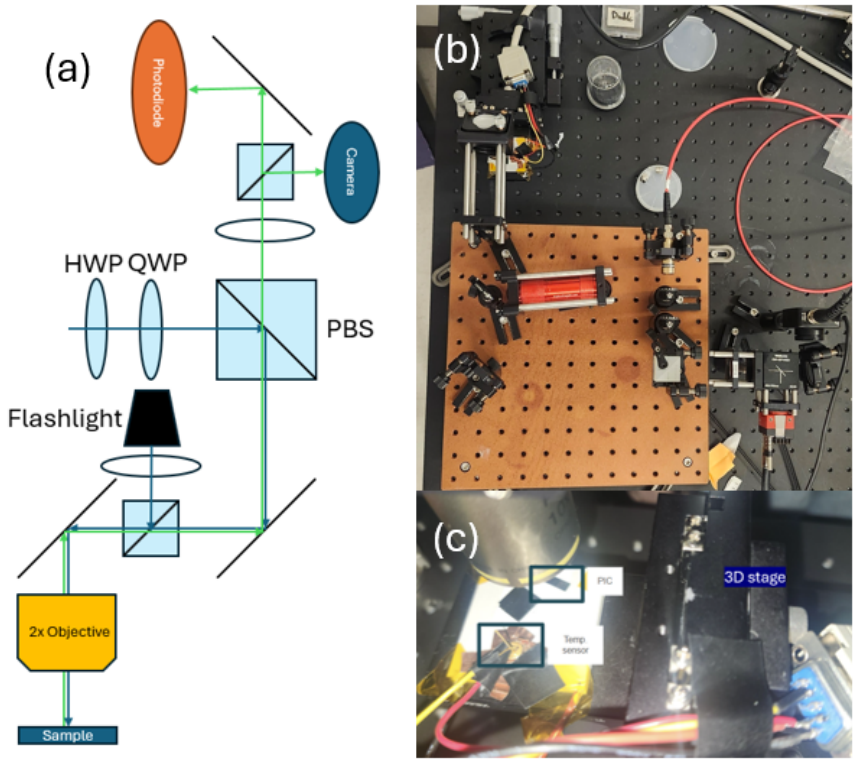

Figure 4.2: (a) Schematic and (b) photograph of the optical setup used to characterize the PIC at 729 nm. The input beam passes through a half-wave plate (HWP) and a quarter-wave plate (QWP) to match the polarization required by the grating couplers. A 2× objective focuses the beam onto the chip surface. Transmitted light is monitored simultaneously by a photodiode for real-time power measurements and a camera for chip imaging, enabling both alignment and coupling efficiency characterization. A flashlight allows for white-light imaging of the chip surface. (c) Photograph of the PIC mounted on a chip carrier with a Thorlabs TECH8 thermoelectric element and AD590 temperature transducer for chip temperature stabilization, used to thermally tune the ring resonators into alignment with the 729 nm laser. The entire assembly is mounted on a three-axis translation stage to achieve precise spatial overlap between the focused input beam and the on-chip grating couplers.

using a thermoelectric cooler (TEC) mounted beneath the chip carrier (Fig. 4.2c). A Thorlabs TECH8 single-stage heating element, paired with an AD590 thermistor affixed to the chip, provides local temperature measurement and feeds a PID controller that stabilizes the chip to a user-defined setpoint. To observe the thermal resonance shift, we attempted to scan the Toptica laser frequency using a triangular piezo-voltage waveform. However, the laser's tunable range proved insufficient to span the resonance-to-resonance wavelength interval required by the thermal tuning scheme (> 0.1 nm). As a result, full thermal characterization of the resonator alignment was not completed at this stage, and we proceeded to PCB integration for FPGA control, as described in the following section.

4.3 Next Steps: FPGA Integration and Experimental Application

The characterization work presented above establishes that the PIC can be efficiently coupled at the target wavelength. The remaining steps to transform this platform into a functional gate-driving system are twofold: integrating fast electronic control via an FPGA, and deploying the system alongside an operational trapped-ion experiment.

FPGA control. The next phase is to interface the PIC with an FPGA control board that drives the fast electro-optic modulators described in Section 4.1. This requires a custom printed circuit board (PCB) routing voltage control lines from the PIC to the FPGA's digital output channels. To minimize signal distortion at nanosecond timescales, the PIC will be diced from the wafer and wire-bonded directly to the PCB, providing low-inductance electrical connections. The DC control firmware has been implemented [cite], while the RF component is currently being developed by a collaborator.

Integration with a trapped-ion experiment. With FPGA control in place, the PIC platform will be deployed alongside a vacuum-chamber-based trapped-ion setup. The grating array output of the PIC will be imaged onto the ion plane through a viewport, delivering the 729 nm gate beam to individual $^{40}Ca^{+}$ ions. Because the PIC is a standalone module connected to the trap only through free-space or fiber optics, it can be paired with any of the trap geometries characterized in Chapter 3 without modification to the light delivery system.

This decoupled architecture provides a clear path toward scaling: additional PIC channels can be added to address more ions, while the trap design is independently optimized for gate fidelity and power dissipation.

Chapter 5

CONCLUSIONS AND OUTLOOK

This thesis addressed two interconnected challenges in scaling laser-based trapped-ion quantum processors: trap geometry design and scalable light delivery.

We developed a quantitative framework for evaluating trap geometries through three figures of merit, harmonicity, trap depth, and radial trap frequency, and applied it to a surface trap, a gnd-surface trap, and a symmetric cross-rf multi-wafer trap. We showed that trap anharmonicity introduces frequency shifts during the Mølmer–Sørensen gate sufficient to limit fidelities below the 99.99% fault-tolerant threshold, establishing harmonicity as a central design metric. The cross-rf trap achieved the highest harmonicity, enabling operation at $q = 0.905$ and yielding a significant improvement in maximum radial trap frequency over the surface trap for the same drive amplitude (6.12 MHz vs. 1.00 MHz), with an estimated power reduction of over four orders of magnitude for a target frequency of $2\pi \times 10$ MHz and a nearly order-of-magnitude lower expected heating rate. The gnd-surface trap offered more modest gains with significantly simpler fabrication.

In parallel, we couple a silicon nitride photonic integrated circuit operating at 729 nm as a scalable platform for laser delivery to $^{40}Ca^{+}$ ions. We demonstrated fiber-to-chip coupling, setup for thermal tuning of ring resonators to a frequency-stabilized laser, and verified transmission through both the resonator and grating array outputs. The two-stage control architecture, slow thermal alignment combined with fast electro-optic modulation on nanosecond timescales, provides the precision and speed required for high-fidelity gate operations, while the standalone design decouples the light delivery system from the trap geometry.

Looking ahead, the comparative analysis of the provided FoM enables systematic progress on the optimization of scalable trap geometry. For the PIC, the immediate next step is FPGA integration for programmable fast modulation, followed by scaling to multiple independently controlled channels. The goal is to run two experiments, one with a gnd-surface trap with

trap-integrated optical access and another with the PIC of 16-channels for multi-qubit operations on a linear ion chain. Both of these future experiments can open the door for further evaluation of the scalability of each engineering perspective and allow for further advancement of utility-scale trapped-ion systems.

BIBLIOGRAPHY

[1] Le Minh Anh Nguyen, Brant Bowers, and Sara Mouradian. The effect of trap design on the scalability of trapped-ion quantum technologies. *Entropy*, 27(6), 2025.

[2] Adrian J. Menssen, Artur Hermans, Ian Christen, Thomas Propson, Chao Li, Andrew J. Leenheer, Matthew Zimmermann, Mark Dong, Hugo Larocque, Hamza Raniwala, Gerald Gilbert, Matt Eichenfield, and Dirk R. Englund. Scalable photonic integrated circuits for high-fidelity light control. *Optica*, 10(10):1366–1372, Oct 2023.

[3] Sujay B. Desai, Surabhi R. Madhvapathy, Angada B. Sachid, Juan Pablo Llinas, Qingxiao Wang, Geun Ho Ahn, Gregory Pitner, Moon J. Kim, Jeffrey Bokor, Chenming Hu, H.-S. Philip Wong, and Ali Javey. Mos₂ transistors with 1-nanometer gate lengths. *Science*, 354(6308):99–102, 2016.

[4] Peng Zhou, Wenzhong Bao, et al. A RISC-V 32-bit microprocessor based on two-dimensional semiconductors. *Nature*, April 2025.

[5] Richard P. Feynman. Simulating physics with computers. *International Journal of Theoretical Physics*, 21:467–488, 1982.

[6] John Preskill. Quantum computing and the entanglement frontier, 2012.

[7] Robert Huang, Jarrod McClean, John Preskill, and Soonwon Choi. The vast world of quantum advantage. *ArXiv*, 2025.

[8] Olivia Lanes, Mourad Beji, Antonio D. Corcoles, Constantin Dalyac, Jay M. Gambetta, Loic Henriet, Ali Javadi-Abhari, Abhinav Kandala, Antonio Mezzacapo, Christopher Porter, Sarah Sheldon, John Watrous, Christa Zoufal, Alexandre Dauphin, and Borja Peropadre. A framework for quantum advantage, 2025.

[9] David P. DiVincenzo. Topics in quantum computers, 1996.

[10] Peter W. Shor. Scheme for reducing decoherence in quantum computer memory. *Phys. Rev. A*, 52:R2493–R2496, 1995.

[11] Andrew M. Steane. Error correcting codes in quantum theory. *Phys. Rev. Lett.*, 77:793–797, 1996.

[12] Alexei Yu. Kitaev. Fault-tolerant quantum computation by anyons. *Ann. Phys.*, 303:2–30, 2003.

[13] Lukas Postler, Friederike Butt, Ivan Pogorelov, Christian D. Marciniak, Sascha Heußen, Rainer Blatt, Philipp Schindler, Manuel Rispler, Markus Müller, and Thomas Monz. Demonstration of fault-tolerant steane quantum error correction. *PRX Quantum*, 5:030326, Aug 2024.

[14] Rajeev Acharya et al. Quantum error correction below the surface code threshold. *Nature*, 638:920–926, 2024. Google Quantum AI.

[15] Andrew D. Ludlow, Martin M. Boyd, Jun Ye, E. Peik, and P. O. Schmidt. Optical atomic clocks. *Rev. Mod. Phys.*, 87:637–701, Jun 2015.

[16] Kevin A. Gilmore, Matthew Affolter, Robert J. Lewis-Swan, Diego Barberena, Elena Jordan, Ana Maria Rey, and John J. Bollinger. Quantum-enhanced sensing of displacements and electric fields with two-dimensional trapped-ion crystals. *Science*, 373(6555):673–678, 2021.

[17] R. Blatt and C. F. Roos. Quantum simulations with trapped ions. *Nat. Phys.*, 8:277–284, 2012.

[18] D. J. Wineland, M. Barrett, J. Britton, J. Chiaverini, B. DeMarco, W. M. Itano, B. Jelenković, C. Langer, D. Leibfried, V. Meyer, T. Rosenband, and T. Schätz. Quantum information processing with trapped ions. *Philosophical Transactions of the Royal Society of London. Series A: Mathematical, Physical and Engineering Sciences*, 361(1808):1349–1361, jul 2003.

[19] Philipp Schindler, Daniel Nigg, Thomas Monz, Julio T Barreiro, Esteban Martinez, Shannon X Wang, Stephan Quint, Matthias F Brandl, Volckmar Nebendahl, Christian F Roos, Michael Chwalla, Markus Hennrich, and Rainer Blatt. A quantum information processor with trapped ions. *New Journal of Physics*, 15(12):123012, dec 2013.

[20] Fangzhao Alex An, Anthony Ransford, Andrew Schaffer, Lucas R. Sletten, John Gaebler, James Hostetter, and Grahame Vittorini. High fidelity state preparation and measurement of ion hyperfine qubits with i 1/2. *Physical Review Letters*, 129(13), sep 2022.

[21] C. J. Ballance, T. P. Harty, N. M. Linke, M. A. Sepiol, and D. M. Lucas. High-fidelity quantum logic gates using trapped-ion hyperfine qubits. *Phys. Rev. Lett.*, 117:060504, Aug 2016.

[22] Craig R. Clark, Holly N. Tinkey, Brian C. Sawyer, Adam M. Meier, Karl A. Burkhardt, Christopher M. Seck, Christopher M. Shappert, Nicholas D. Guise, Curtis E. Volin, Spencer D. Fallek, Harley T. Hayden, Wade G. Rellergert, and Kenton R. Brown. High-fidelity bell-state preparation with $^{40}ca^{+}$ optical qubits. *Phys. Rev. Lett.*, 127:130505, 2021.

[23] Brian C. Sawyer and Kenton R. Brown. Wavelength-insensitive, multispecies entangling gate for group-2 atomic ions. *Phys. Rev. A*, 103:022427, 2021.

[24] C. Ospelkaus, U. Warring, Y. Colombe, K. R. Brown, J. M. Amini, D. Leibfried, and D. J. Wineland. Microwave quantum logic gates for trapped ions. *Nature*, 476(7359):181–184, 2011.

[25] M. A. Weber, M. F. Gely, R. K. Hanley, T. P. Harty, A. D. Leu, C. M. Löschnauer, D. P. Nadlinger, and D. M. Lucas. Robust and fast microwave-driven quantum logic for trapped-ion qubits. *Physical Review A*, 110(1), 2024.

[26] C. M. Löschnauer et al. Scalable, high-fidelity all-electronic control of trapped-ion qubits. *arXiv*, 2024.

[27] Michael A. Nielsen and Isaac L. Chuang. *Quantum Computation and Quantum Information: 10th Anniversary Edition*. Cambridge University Press, 2010.

[28] J. J. Sakurai and Jim Napolitano. *Modern Quantum Mechanics*. Cambridge University Press, 3 edition, 2020.

[29] Colin D. Bruzewicz, John Chiaverini, Robert McConnell, and Jeremy M. Sage. Trapped-ion quantum computing: Progress and challenges. *Applied Physics Reviews*, 6(2):021314, 05 2019.

[30] P. A. Barton, C. J. S. Donald, D. M. Lucas, D. A. Stevens, A. M. Steane, and D. N. Stacey. Measurement of the lifetime of the $3d^2D_{5/2}$ state in $^{40}ca^+$. *Phys. Rev. A*, 62:032503, Aug 2000.

[31] Wolfgang Paul. Electromagnetic traps for charged and neutral particles. *Rev. Mod. Phys.*, 62:531–540, 1990.

[32] Pradip K. Ghosh. *Ion Traps*. A Clarendon Press Publication, 1995.

[33] Chris Brimacombe, Robert M. Corless, and Mair Zamir. Computation and applications of mathieu functions: A historical perspective. *SIAM Review*, 63(4):653–720, 2021.

[34] Christopher C. Gerry and Peter L. Knight. *Introductory Quantum Optics*. Cambridge University Press, 2005.

[35] D. Leibfried, R. Blatt, C. Monroe, and D. Wineland. Quantum dynamics of single trapped ions. *Rev. Mod. Phys.*, 75:281–324, Mar 2003.

[36] Anders Sørensen and Klaus Mølmer. Quantum computation with ions in thermal motion. *Physical Review Letters*, 82:1971–1974, 1999.

[37] Klaus Mølmer and Anders Sørensen. Multiparticle entanglement of hot trapped ions. *Physical Review Letters*, 82:1835–1838, 1999.

[38] Wilhelm Magnus. On the exponential solution of differential equations for a linear operator. *Communications on Pure and Applied Mathematics*, 7:649–673, 1954.

[39] R. Tyler Sutherland, Qian Yu, Kristin M. Beck, and Hartmut Häffner. One- and two-qubit gate infidelities due to motional errors in trapped ions and electrons. *Phys. Rev. A*, 105:022437, Feb 2022.

[40] J. Chiaverini, R. B. Blakestad, J. Britton, J. D. Jost, C. Langer, D. Leibfried, R. Ozeri, and D. J. Wineland. Surface-electrode architecture for ion-trap quantum information processing. *Quantum Information and Computation*, 5(6):419–439, 2005.

[41] J. Zhang, G. Pagano, P. W. Hess, A. Kyprianidis, P. Becker, H. Kaplan, A. V. Gorshkov, Z.-X. Gong, and C. Monroe. Observation of a many-body dynamical phase transition with a 53-qubit quantum simulator. *Nature*, 551(7682):601–604, nov 2017.

[42] J. M. Pino, J. M. Dreiling, C. Figgatt, J. P. Gaebler, S. A. Moses, M. S. Allman, C. H. Baldwin, M. Foss-Feig, D. Hayes, K. Mayer, C. Ryan-Anderson, and B. Neyenhuis. Demonstration of the trapped-ion quantum ccd computer architecture. *Nature*, 592(7853):209–213, 2021.

[43] I. Pogorelov, T. Feldker, Ch. D. Marciniak, L. Postler, G. Jacob, O. Krieglsteiner, V. Podlesnic, M. Meth, V. Negnevitsky, M. Stadler, B. Höfer, C. Wächter, K. Lakhmanskiy, R. Blatt, P. Schindler, and T. Monz. Compact ion-trap quantum computing demonstrator. *PRX Quantum*, 2:020343, Jun 2021.

[44] S.A. Moses, C.H. Baldwin, M.S. Allman, R. Ancona, L. Ascarrunz, C. Barnes, J. Bartolotta, B. Bjork, P. Blanchard, M. Bohn, J.G. Bohnet, N.C. Brown, N.Q. Burdick, W.C. Burton, S.L. Campbell, J.P. Campora, C. Carron, J. Chambers, J.W. Chan, Y.H. Chen, A. Chernoguzov, E. Chertkov, J. Colina, J.P. Curtis, R. Daniel, M. DeCross, D. Deen, C. Delaney, J.M. Dreiling, C.T. Ertsgaard, J. Esposito, B. Estey, M. Fabrikant, C. Figgatt, C. Foltz, M. Foss-Feig, D. Francois, J.P. Gaebler, T.M. Gatterman, C.N. Gilbreth, J. Giles, E. Glynn, A. Hall, A.M. Hankin, A. Hansen, D. Hayes, B. Higashi, I.M. Hoffman, B. Horning, J.J. Hout, R. Jacobs, J. Johansen, L. Jones, J. Karcz, T. Klein, P. Lauria, P. Lee, D. Liefer, S.T. Lu, D. Lucchetti, C. Lytle, A. Malm, M. Matheny, B. Mathewson, K. Mayer, D.B. Miller, M. Mills, B. Neyenhuis, L. Nugent, S. Olson, J. Parks, G.N. Price, Z. Price, M. Pugh, A. Ransford, A.P. Reed, C. Roman, M. Rowe, C. Ryan-Anderson, S. Sanders, J. Sedlacek, P. Shevchuk, P. Siegfried, T. Skripka, B. Spaun, R.T. Sprenkle, R.P. Stutz, M. Swallows, R.I. Tobey, A. Tran, T. Tran, E. Vogt, C. Volin, J. Walker, A.M. Zolot, and J.M. Pino. A race-track trapped-ion quantum processor. *Physical Review X*, 13(4), 2023.

[45] Jwo-Sy Chen, Erik Nielsen, Matthew Ebert, Volkan Inlek, Kenneth Wright, Vandiver Chaplin, Andrii Maksymov, Eduardo Páez, Amrit Poudel, Peter Maunz, and John Gamble. Benchmarking a trapped-ion quantum computer with 30 qubits. *Quantum*, 8:1516, nov 2024.

[46] Ben W. Reichardt, David Aasen, Rui Chao, Alex Chernoguzov, Wim van Dam, John P. Gaebler, Dan Gresh, Dominic Lucchetti, Michael Mills, Steven A. Moses, Brian Neyenhuis, Adam Paetznick, Andres Paz, Peter E. Siegfried, Marcus P. da Silva, Krysta M. Svore, Zhenghan Wang, and Matt Zanner. Demonstration of quantum computation and error correction with a tesseract code. *arXiv*, 2024.

[47] C. Zhang, F. Pokorny, W. Li, et al. Submicrosecond entangling gate between trapped ions via rydberg interaction. *Nature*, 580:345–349, 2020.

[48] Sagnik Saha, Mikhail Shalaev, Jameson O'Reilly, Isabella Goetting, George Toh, Ashish Kalakuntla, Yichao Yu, and Christopher Monroe. High-fidelity remote entanglement of trapped atoms mediated by time-bin photons. *Nat. Commun.*, 16(2533):1–8, mar 2025.

[49] S. Saner, O. Băzăvan, M. Minder, P. Drmota, D. J. Webb, G. Araneda, R. Srinivas, D. M. Lucas, and C. J. Ballance. Breaking the entangling gate speed limit for trapped-ion qubits using a phase-stable standing wave. *Phys. Rev. Lett.*, 131:220601, Dec 2023.

[50] V. M. Schäfer, C. J. Ballance, K. Thirumalai, L. J. Stephenson, T. G. Ballance, A. M. Steane, and D. M. Lucas. Fast quantum logic gates with trapped-ion qubits. *Nature*, 555(7694):75–78, mar 2018.

[51] A. Steane, C. F. Roos, D. Stevens, A. Mundt, D. Leibfried, F. Schmidt-Kaler, and R. Blatt. Speed of ion-trap quantum-information processors. *Phys. Rev. A*, 62:042305, 2000.

[52] M. Brownnutt, M. Kumph, P. Rabl, and R. Blatt. Ion-trap measurements of electric-field noise near surfaces. *Rev. Mod. Phys.*, 87:1419–1482, 2015.

[53] C. E. Pearson, D. R. Leibrandt, W. S. Bakr, W. J. Mallard, K. R. Brown, and I. L. Chuang. Experimental investigation of planar ion traps. *Phys. Rev. A*, 73:032307, Mar 2006.

[54] D. T. C. Allcock, J. A. Sherman, D. N. Stacey, A. H. Burrell, M. J. Curtis, G. Imreh, N. M. Linke, D. J. Szwer, S. C. Webster, A. M. Steane, and D. M. Lucas. Implementation of a symmetric surface-electrode ion trap with field compensation using a modulated Raman effect. *New J. Phys.*, 12(5):053026, may 2010.

[55] Seokjun Hong, Minjae Lee, Hongjin Cheon, Taehyun Kim, and Dong-il Cho. Guidelines for designing surface ion traps using the boundary element method. *Sensors*, 16(5), 2016.

[56] S. Charles Doret, Jason M. Amini, Kenneth Wright, Curtis Volin, Tyler Killian, Arkadas Ozakin, Douglas Denison, Harley Hayden, C.-S. Pai, Richart E. Slusher, and Alexa W. Harter. Controlling trapping potentials and stray electric fields in a microfabricated ion trap through design and compensation. *New J. Phys.*, 14(7):073012, jul 2012.

[57] D. L. Moehring, C. Highstrete, D. Stick, K. M. Fortier, R. Haltli, C. Tigges, and M. G. Blain. Design, fabrication and experimental demonstration of junction surface ion traps. *New J. Phys.*, 13(7):075018, jul 2011.

[58] Kenneth Wright, Jason M. Amini, Daniel L. Faircloth, Curtis Volin, S. Charles Doret, Harley Hayden, C.-S. Pai, David W. Landgren, Douglas Denison, Tyler Killian, Richart E. Slusher, and Alexa W. Harter. Reliable transport through a microfabricated X-junction surface-electrode ion trap. *New J. Phys.*, 15(3):033004, mar 2013.

[59] A. J. Rasmusson. A high motional frequency ion trapping regime for quantum information science, 2026.

[60] Karan K. Mehta, Colin D. Bruzewicz, Robert McConnell, Rajeev J. Ram, Jeremy M. Sage, and John Chiaverini. Integrated optical addressing of an ion qubit. *Nat. Nanotechnol.*, 11:1066–1070, 2016.

[61] Peter Lukas Wilhelm Maunz. High optical access trap 2.0. Technical report, Sandia National Lab. (SNL-NM), Albuquerque, NM (United States), 01 2016.

[62] Ilya Gerasin, Nikita Zhadnov, Konstantin Kudeyarov, Ksienia Khabarova, Nikolay Kolachevsky, and Ilya Semerikov. Optimized surface ion trap design for tight confinement and separation of ion chains. *Quantum Reports*, 6(3):442–451, 2024.

[63] C. Marquet, F. Schmidt-Kaler, and D.F.V. James. Phonon-phonon interactions due to non-linear effects in a linear ion trap. *Applied Physics B: Lasers and Optics*, 76(3):199–208, mar 2003.

[64] J. P. Home, D. Hanneke, J. D. Jost, D. Leibfried, and D. J. Wineland. Normal modes of trapped ions in the presence of anharmonic trap potentials. *New J. Phys.*, 13(7):073026, 2011.

[65] Yukai Wu, Sheng-Tao Wang, and L.-M. Duan. Noise analysis for high-fidelity quantum entangling gates in an anharmonic linear Paul trap. *Phys. Rev. A*, 97(6):062325, 2018.

[66] R. Alheit, X. Z. Chu, M. Hoefer, M. Holzki, G. Werth, and R. Blümel. Nonlinear collective oscillations of an ion cloud in a paul trap. *Phys. Rev. A*, 56:4023–4031, Nov 1997.

[67] M. A. N. Razvi, X. Z. Chu, R. Alheit, G. Werth, and R. Blümel. Fractional frequency collective parametric resonances of an ion cloud in a paul trap. *Phys. Rev. A*, 58:R34–R37, Jul 1998.

[68] A. Drakoudis, M. Söllner, and G. Werth. Instabilities of ion motion in a linear paul trap. *International Journal of Mass Spectrometry*, 252(1):61–68, 2006.

[69] Gebhard Littich. Electrostatic control and transport of ions on a planar trap for. quantum information processing. Master's thesis, ETH Zurich, 2011.

[70] Jeremy M. Sage, Andrew J. Kerman, and John Chiaverini. Loading of a surface-electrode ion trap from a remote, precooled source. *Phys. Rev. A*, 86(1):013417, jul 2012.

[71] H.G. Dehmelt. *Radiofrequency Spectroscopy of Stored Ions I: Storage*, volume 3 of *Advances in Atomic and Molecular Physics*. Academic Press, 1968.

[72] Shuqi Xu, Xiaoxing Xia, Qian Yu, Sumanta Khan, Eli Megidish, Bingran You, Boerge Hemmerling, Andrew Jayich, Juergen Biener, and Hartmut Häffner. 3d-printed micro ion trap technology for scalable quantum information processing. *arXiv*, 2023.

[73] R. C. Sterling, M. D. Hughes, C. J. Mellor, and W. K. Hensinger. Increased surface flashover voltage in microfabricated devices. *Applied Physics Letters*, 103(14), 2013.

[74] Keith G. Ray, Brenda M. Rubenstein, Wenze Gu, and Vincenzo Lordi. van der waals-corrected density functional study of electric field noise heating in ion traps caused by electrode surface adsorbates. *New Journal of Physics*, 21(5):053043, 2019.

[75] D. A. Hite, K. S. McKay, and D. P. Pappas. Surface science motivated by heating of trapped ions from the quantum ground state. *New Journal of Physics*, 23(10), 2021.

[76] J. I. Cirac and P. Zoller. A scalable quantum computer with ions in an array of microtraps. *Nature*, 2000.

[77] Lakhi Sharma, A. Roy, S. Panja, V. N. Ojha, and S. De. Estimation of the ion-trap assisted electrical loads and resulting BBR shift. *Sci. Rep.*, 8(16884):1–10, November 2018.

[78] J. Chiaverini, R. B. Blakestad, J. Britton, J. D. Jost, C. Langer, D. Leibfried, R. Ozeri, and D. J. Wineland. Surface-Electrode Architecture for Ion-Trap Quantum Information Processing. *arXiv*, January 2005.

[79] J. D. Sterk, M. G. Blain, M. Delaney, R. Haltli, E. Heller, A. L. Holterhoff, T. Jennings, N. Jimenez, A. Kozhanov, and Z. Meinelt. Multi-junction surface ion trap for quantum computing, March 2024. [Online; accessed 19. May 2025].

[80] Zachary Kenneth Meinelt, Matthew Bahr, Patrick Sean Finnegan, Raymond A. Haltli, Matthew Jordan, Benjamin Harrison Klitsner, Tyler Liebsch, Andrew Mounce, Scott Edward Weatherred, and Daniel Lynn Stick. Microfabricated ion traps on sapphire for larger trap areas and higher qubit count. Technical report, Sandia National Lab. (SNL-NM), Albuquerque, NM (United States), 09 2024.

[81] J. M. Amini, H. Uys, J. H. Wesenberg, S. Seidelin, J. Britton, J. J. Bollinger, D. Leibfried, C. Ospelkaus, A. P. VanDevender, and D. J. Wineland. Toward scalable ion traps for quantum information processing. *New J. Phys.*, 12(3):033031, mar 2010.

[82] William Cody Burton, Brian Estey, Ian M. Hoffman, Abigail R. Perry, Curtis Volin, and Gabriel Price. Transport of Multispecies Ion Crystals through a Junction in a Radio-Frequency Paul Trap. *Phys. Rev. Lett.*, 130(17):173202, apr 2023.

[83] G. Shu, G. Vittorini, A. Buikema, C. S. Nichols, C. Volin, D. Stick, and Kenneth R. Brown. Heating rates and ion-motion control in a Y-junction surface-electrode trap. *Phys. Rev. A*, 89(6):062308, jun 2014.

[84] A. Decaroli et al. Design, fabrication and characterization of a micro-fabricated stacked-wafer segmented ion trap with two x-junctions. *Quantum Science and Technology*, 6(4):044001, 2021.

[85] Simon Ragg, Chiara Decaroli, Thomas Lutz, and Jonathan P. Home. Segmented ion-trap fabrication using high precision stacked wafers. *Review of Scientific Instruments*, 90(10), oct 2019.

[86] Guido Wilpers, Patrick See, Patrick Gill, and Alastair G. Sinclair. A monolithic array of three-dimensional ion traps fabricated with conventional semiconductor technology. *Nature Nanotechnology*, 7(9):572–576, 2012.

[87] Sanghyo Park, Milica Notaros, Aseema Mohanty, Donggyu Kim, Jelena Notaros, and Sara Mouradian. Technologies for modulation of visible light and their applications. *Prog. Quantum Electron.*, 97:100534, 2024.

[88] Robert D. Delaney, Lucas R. Sletten, Matthew J. Cich, Brian Estey, Maya I. Fabrikant, David Hayes, Ian M. Hoffman, James Hostetter, Christopher Langer, Steven A. Moses, Abigail R. Perry, Timothy A. Peterson, Andrew Schaffer, Curtis Volin, Grahame Vittorini, and William Cody Burton. Scalable multispecies ion transport in a grid-based surface-electrode trap. *Physical Review X*, 14(4), nov 2024.

[89] Karan K. Mehta, Chi Zhang, Maciej Malinowski, Thanh-Long Nguyen, Martin Stadler, and Jonathan P. Home. Integrated optical multi-ion quantum logic. *Nature*, 586:533–537, 2020.

[90] R. J. Niffenegger, J. Stuart, C. Sorace-Agaskar, D. Kharas, S. Bramhavar, C. D. Bruzewicz, W. Loh, R. T. Maxson, R. McConnell, D. Reens, G. N. West, J. M. Sage, and J. Chiaverini. Integrated multi-wavelength control of an ion qubit. *Nature*, 586:538–542, oct 2020.

[91] Mizuki Shirao, Daniel Klawson, Sara Mouradian, and Ming C. Wu. High efficiency focusing double-etched SiN grating coupler for trapped ion qubit manipulation. *Jpn. J. Appl. Phys.*, 61(SK):SK1002, 2022.

[92] W. K. Hensinger, S. Olmschenk, D. Stick, D. Hucul, M. Yeo, M. Acton, L. Deslauriers, C. Monroe, and J. Rabchuk. T-junction ion trap array for two-dimensional ion shuttling, storage, and manipulation. *Appl. Phys. Lett.*, 88(3):034101, jan 2006.

[93] R. B. Blakestad, C. Ospelkaus, A. P. VanDevender, J. M. Amini, J. Britton, D. Leibfried, and D. J. Wineland. High-Fidelity Transport of Trapped-Ion Qubits through an **X**-Junction Trap Array. *Phys. Rev. Lett.*, 102(15):153002, apr 2009.

[94] R. B. Blakestad, C. Ospelkaus, A. P. VanDevender, J. H. Wesenberg, M. J. Biercuk, D. Leibfried, and D. J. Wineland. Near-ground-state transport of trapped-ion qubits through a multidimensional array. *Phys. Rev. A*, 84(3):032314, sep 2011.

[95] J. I. Cirac and P. Zoller. Quantum computations with cold trapped ions. *Phys. Rev. Lett.*, 74:4091–4094, 1995.

[96] Joonhyuk Kwon, William J. Setzer, Michael Gehl, Nicholas Karl, Jay Van Der Wall, Ryan Law, Matthew G. Blain, Daniel Stick, and Hayden J. McGuinness. Multi-site integrated optical addressing of trapped ions. *Nature Communications*, 15(1), May 2024.

[97] C. W. Hogle, D. Dominguez, M. Dong, A. Leenheer, H. J. McGuinness, B. P. Ruzic, M. Eichenfield, and D. Stick. High-fidelity trapped-ion qubit operations with scalable photonic modulators. *npj Quantum Inf.*, 9(74):1–6, jul 2023.

[98] A. Quinn, M. Brown, T. J. Gardner, and D. T. C. Allcock. Geometries and fabrication methods for 3d printing ion traps. *arXiv*, 2022.

[99] Michael E. Beverland, Prakash Murali, Matthias Troyer, Krysta M. Svore, Torsten Hoefler, Vadym Kliuchnikov, Guang Hao Low, Mathias Soeken, Aarthi Sundaram, and Alexander Vaschillo. Assessing requirements to scale to practical quantum advantage. *arXiv*, 2022.

[100] Pei Jiang Low. Tolerable experimental imperfections for a quadrupole blade ion trap and practical qudit gates with trapped ions. Master's thesis, University of Waterloo, 2019. Master's thesis.

[101] C. L. Degen, F. Reinhard, and P. Cappellaro. Quantum sensing. *Rev. Mod. Phys.*, 89:035002, Jul 2017.

[102] F. W. Knollmann, E. Clements, P. T. Callahan, M. Gehl, J. D. Hunker, T. Mahony, R. McConnell, R. Swint, C. Sorace-Agaskar, I. L. Chuang, J. Chiaverini, and D. Stick. Integrated photonic structures for photon-mediated entanglement of trapped ions. *Optica Quantum*, 2(4):230, August 2024.

[103] Da An, Clemens Matthiesen, Ahmed Abdelrahman, Maya Berlin-Udi, Dylan Gorman, Sönke Möller, Erik Urban, and Hartmut Häffner. Surface trap with dc-tunable ion-electrode distance. *Review of Scientific Instruments*, 89(9):093102, 09 2018.

[104] Vlad Negnevitsky. *Feedback-stabilised quantum states in a mixed-species ion system.* Doctoral thesis, ETH Zurich, Zurich, 2018-09-27.

[105] Hsin-Yuan Huang, Michael Broughton, Jordan Cotler, Sitan Chen, Jerry Li, Masoud Mohseni, Hartmut Neven, Ryan Babbush, Richard Kueng, John Preskill, and Jarrod R. McClean. Quantum advantage in learning from experiments. *Science*, 376(6598):1182–1186, June 2022.

[106] C. Monroe and J. Kim. Scaling the ion trap quantum processor. *Science*, 339(6124):1164–1169, 2013.

[107] Zain Mehdi, Alexander K. Ratcliffe, and Joseph J. Hope. Fast entangling gates in long ion chains. *Physical Review Research*, 3(1), January 2021.

[108] R. Tyler Sutherland, Qian Yu, Kristin M. Beck, and Hartmut Häffner. One- and two-qubit gate infidelities due to motional errors in trapped ions and electrons. *Physical Review A*, 105(2), feb 2022.

[109] B. P. Ruzic, T. A. Barrick, J. D. Hunker, R. J. Law, B. K. McFarland, H. J. McGuinness, L. P. Parazzoli, J. D. Sterk, J. W. Van Der Wall, and D. Stick. Entangling-gate error from coherently displaced motional modes of trapped ions. *Physical Review A*, 105(5), May 2022.

[110] S Charles Doret, Jason M Amini, Kenneth Wright, Curtis Volin, Tyler Killian, Arkadas Ozakin, Douglas Denison, Harley Hayden, C-S Pai, Richart E Slusher, and Alexa W Harter. Controlling trapping potentials and stray electric fields in a microfabricated ion trap through design and compensation. *New Journal of Physics*, 14(7):073012, jul 2012.

[111] Kenneth Wright, Jason M Amini, Daniel L Faircloth, Curtis Volin, S Charles Doret, Harley Hayden, C-S Pai, David W Landgren, Douglas Denison, Tyler Killian, Richart E Slusher, and Alexa W Harter. Reliable transport through a microfabricatedx-junction surface-electrode ion trap. *New Journal of Physics*, 15(3):033004, mar 2013.

[112] Masatoshi Kajita. *Ion Traps*. 2053-2563. IOP Publishing, 2022.

[113] S. Auchter, C. Axline, C. Decaroli, M. Valentini, L. Purwin, R. Oswald, R. Matt, E. Aschauer, Y. Colombe, P. Holz, T. Monz, R. Blatt, P. Schindler, C. Rössler, and J. Home. Industrially microfabricated ion trap with 1 ev trap depth, 2022.

[114] J. H. Wesenberg. Electrostatics of surface-electrode ion traps. *Phys. Rev. A*, 78:063410, Dec 2008.

[115] A. M. Steane. Active stabilization, quantum computation, and quantum state synthesis. *Phys. Rev. Lett.*, 78:2252–2255, Mar 1997.

[116] Quantum Metrology. Surface-electrode trap fabrication, n.d. Accessed: 2025-02-20.

[117] D. A. Hite, K. S. McKay, S. Kotler, D. Leibfried, D. J. Wineland, and D. P. Pappas. Measurements of trapped-ion heating rates with exchangeable surfaces in close proximity. *MRS Advances*, 2(41):2189–2197, 2017.

[118] Thomas Strohm, Karen Wintersperger, Florian Dommert, Daniel Basilewitsch, Georg Reuber, Andrey Hoursanov, Thomas Ehmer, Davide Vodola, and Sebastian Luber. Ion-based quantum computing hardware: Performance and end-user perspective, 2024.

[119] M. C. Revelle, M. A. Delaney, R. A. Haltli, E. Heller, C. D. Nordquist, E. Ou, J. Van Der Wall, and S. M. Clark. The roadrunner trap: A qscout device. Technical Report SAND2023-14948, Sandia National Laboratories, 2023.

[120] Chi Zhang, Fabian Pokorny, Weibin Li, Gerard Higgins, Andreas Pöschl, Igor Lesanovsky, and Markus Hennrich. Submicrosecond entangling gate between trapped ions via Rydberg interaction. *Nature*, 580:345–349, apr 2020.

[121] Sergio Blanes, Fernando Casas, José-Angel Oteo, and José Ros. The Magnus expansion and some of its applications. *Physics Reports*, 470:151–238, 2009.

[122] Lukas Postler, Sascha Häußler, Ivan Pogorelov, Manuel Rispler, Thomas Feldker, Michael Meth, Christian D. Marciniak, Rainer Blatt, Markus Müller, Philipp Schindler, and Thomas Monz. Demonstration of fault-tolerant universal quantum gate operations. *Nature*, 605:675–680, 2022.

[123] P. L. Knight, E. A. Hinds, M. B. Plenio, D. J. Wineland, M. Barrett, J. Britton, J. Chiaverini, B. DeMarco, W. M. Itano, B. Jelenković, C. Langer, D. Leibfried, V. Meyer, T. Rosenband, and T. Schätz. Quantum information processing with trapped ions. *Philosophical Transactions of the Royal Society A: Mathematical, Physical and Engineering Sciences*, 361(1808):1349–1361, 07 2003.

Appendix A

USEFUL MATHEMATICAL DEFINITIONS

A.1 Pauli Matrices

The Pauli matrices are a set of three 2×2 complex matrices that correspond to orthonormal axes on the Bloch sphere, as shown in Fig. 2.1.a. They are given by

$$\sigma_x = \begin{pmatrix} 0 & 1 \\ 1 & 0 \end{pmatrix}, \qquad \sigma_y = \begin{pmatrix} 0 & -i \\ i & 0 \end{pmatrix}, \qquad \sigma_z = \begin{pmatrix} 1 & 0 \\ 0 & -1 \end{pmatrix}. \tag{A.1}$$

These matrices satisfy

$$\det(\sigma_k) = -1, \qquad \mathrm{Tr}(\sigma_k) = 0, \tag{A.2}$$

and therefore are traceless and have unit magnitude determinant.

The Pauli matrices obey the important product relation

$$\sigma_i \sigma_j = \delta_{ij} \hat{I} + i \varepsilon_{ijk} \sigma_k, \tag{A.3}$$

where $\hat{I}$ is the 2×2 identity matrix. The indices i, j, and k label the Cartesian directions x, y, and z, and therefore correspond to the three Pauli matrices σ_x, σ_y, and σ_z. Here, δ_{ij} is the Kronecker delta and ε_{ijk} is the three-dimensional Levi–Civita symbol. The Kronecker delta is defined as

$$\delta_{ij} = \begin{cases} 1 & \text{if } i = j, \\ 0 & \text{if } i \neq j, \end{cases} \tag{A.4}$$

and the Levi-Civita symbol is given by

$$\varepsilon_{ijk} = \begin{cases} +1 & \text{for even permutations of } (x, y, z), \\ -1 & \text{for odd permutations of } (x, y, z), \\ 0 & \text{if any two indices are equal.} \end{cases} \tag{A.5}$$

The Pauli matrices are involutory, satisfying

$$\sigma_k^2 = \hat{I}. \tag{A.6}$$

This property leads to an important exponential identity, which can be derived using the Taylor expansion

$$e^x = \sum_{n=0}^{\infty} \frac{x^n}{n!}. \tag{A.7}$$

Using $\sigma_k^2 = \hat{I}$, one finds

$$e^{i\theta\sigma_k} = \cos\theta\,\hat{I} + i\sin\theta\,\sigma_k. \tag{A.8}$$

An important property of the Pauli matrices is given by their commutation and anti-commutation relations. They satisfy

$$[\sigma_j, \sigma_k] = 2i\varepsilon_{jki}\sigma_i, \tag{A.9}$$

and

$$\{\sigma_j, \sigma_k\} = 2\delta_{jk}\hat{I}. \tag{A.10}$$

Each Pauli matrix has two eigenvalues, $+1$ and -1, corresponding to the two possible measurement outcomes of a spin-$\frac{1}{2}$ system along a given axis. The eigenvalue equation for a Pauli matrix σ_k is given by

$$\sigma_k\,|\psi\rangle = \lambda\,|\psi\rangle\,, \tag{A.11}$$

where $\lambda \in \{+1, -1\}$ is the eigenvalue and $|\psi\rangle$ is the corresponding eigenvector.

For the operator σ_z, which forms the computational basis commonly used in quantum information theory,

$$|0\rangle = \begin{pmatrix} 1 \\ 0 \end{pmatrix}, \qquad |1\rangle = \begin{pmatrix} 0 \\ 1 \end{pmatrix}, \tag{A.12}$$

$$\sigma_z\,|0\rangle = +\,|0\rangle\,, \qquad \sigma_z\,|1\rangle = -\,|1\rangle\,. \tag{A.13}$$

Similarly, for σ_x,

$$|+\rangle_x = \frac{1}{\sqrt{2}}\begin{pmatrix} 1 \\ 1 \end{pmatrix}, \qquad |-\rangle_x = \frac{1}{\sqrt{2}}\begin{pmatrix} 1 \\ -1 \end{pmatrix}, \tag{A.14}$$

$$\sigma_x\,|\pm\rangle_x = \pm\,|\pm\rangle_x\,. \tag{A.15}$$

and, for σ_y,

$$|+\rangle_y = \frac{1}{\sqrt{2}}\begin{pmatrix} 1 \\ i \end{pmatrix}, \qquad |-\rangle_y = \frac{1}{\sqrt{2}}\begin{pmatrix} 1 \\ -i \end{pmatrix}, \tag{A.16}$$

$$\sigma_y \left|\pm\right\rangle_y = \pm \left|\pm\right\rangle_y . \tag{A.17}$$

The eigenstates of different Pauli operators are mutually unbiased. For example, an eigenstate of σ_z has equal probability of being measured in either eigenstate of σ_x or σ_y. More generally, for an arbitrary unit vector $\mathbf{n}$, the operator

$$\sigma_{\mathbf{n}} = \mathbf{n} \cdot \boldsymbol{\sigma} = n_x \sigma_x + n_y \sigma_y + n_z \sigma_z \tag{A.18}$$

has eigenvalues ± 1, with eigenvectors corresponding to quantum states polarized along the direction $\mathbf{n}$ on the Bloch sphere.

The Pauli operators $\hat{\sigma}_x$ and $\hat{\sigma}_y$ arises from the two-level restriction:

$$\hat{\sigma}_+ = \left|1\right\rangle \left\langle 0\right|, \quad \hat{\sigma}_- = \left|0\right\rangle \left\langle 1\right| , \tag{A.19}$$

$$\rightarrow \quad \hat{\sigma}_x = \hat{\sigma}_- + \hat{\sigma}_+, \quad \hat{\sigma}_y = i(\hat{\sigma}_- - \hat{\sigma}_+) \tag{A.20}$$

This gives the identity

$$\hat{\sigma}_x \cos\omega_{01} t - \hat{\sigma}_y \sin\omega_{01} t = e^{i\omega_{01} t} \hat{\sigma}_+ + ^{-i\omega_{01} t} \hat{\sigma}_- \tag{A.21}$$